Universal polymeric-to-colloidal transition in melts of hairy nanoparticles

Daniele Parisi, Eileen Buenning, Nikolaos Kalafatakis, Leo Gury, Brian C Benicewicz, Mario Gauthier, Michel Cloitre, Michael Rubinstein, Sanat K Kumar, Dimitris Vlassopoulos

Universal polymeric-to-colloidal transition in melts of hairy nanoparticles

Daniele Parisi,[1] Eileen Buenning,[2] Nikolaos Kalafatakis,[1] Leo Gury,[1,3] Brian C. Benicewicz,[4] Mario Gauthier[5], Michel Cloitre,[3] Michael Rubinstein,[6,7] Sanat K. Kumar,[2] Dimitris Vlassopoulos[1]

[1] University of Crete, Department of Materials Science and Technology, and FORTH, Institute of Electronic Structure and Laser, Heraklion, Greece.

[2] Department of Chemical Engineering, Columbia University, New York, NY 10025, USA.

[3] Molecular, Macromolecular Chemistry and Materials, ESPCI Paris, CNRS, PSL Research University, 75005 Paris, France

[4] Department of Chemistry and Biochemistry, University of South Carolina, Columbia, SC 29208, USA

[5] Department of Chemistry, Institute for Polymer Research, University of Waterloo, Waterloo, Ontario, Canada N2L 3G1

[6] Departments of Mechanical Engineering and Materials Science, Biomedical Engineering, Chemistry, and Physics, Duke University, Durham, NC 27708, USA

[7]Institute for Chemical Reaction Design and Discovery (WPI-ICReDD), Hokkaido University, Sapporo 001-0021, Japan

Abstract

Two different classes of hairy self-suspended nanoparticles in the melt state, polymer-grafted nanoparticles (GNPs) and star polymers, are shown to display universal dynamic behavior across a broad range of parameter space. Linear viscoelastic measurements on well-characterized silica-poly(methyl acrylate) GNPs at fixed core radius (R_{core}) and grafting density (or number of arms f), but varying arm degree of polymerization (N_{arm}) show two distinctly different regimes of response. A colloidal Regime I at small N_{arm} (large core volume fraction), with a predominant low-frequency solid-like colloidal plateau and ultraslow relaxation, and a polymeric Regime II at large N_{arm} (small core volume fractions), with a response dominated by the star-like relaxation of partially interpenetrated arms. The transition between the two regimes is marked by a cross-over where both polymeric and colloidal modes are discerned albeit without a distinct colloidal plateau. Similarly, polybutadiene multiarm stars also exhibit the colloidal response of Regime I at very

large f and small N_{arm}. The star arm relaxation model and a simple scaling model of nanoparticle escape from the cage of neighbors by overcoming a hopping potential barrier due to their elastic deformation, describe quantitatively the linear response of the polymeric and colloidal regimes, respectively, in all these cases. The dynamic behavior of hairy nanoparticles of different chemistry and molecular characteristics, investigated here and reported in the literature, can be mapped onto a universal dynamic diagram of $\frac{f}{(R_{core}^3/v_0)^{1/4}}$ as a function of $\frac{N_{arm}v_0 f}{R_{core}^3}$, where v_0 is the monomeric volume. In this diagram, the two regimes are separated by a line where the hopping potential ΔU_{hop} is equal to the thermal energy, k_BT. ΔU_{hop} can be expressed as a function of the overcrowding parameter x, i.e. the ratio of f to the maximum number of unperturbed chains with N_{arm} that can fill the volume occupied by the polymeric corona, hence this crossing is shown to occur when x=1. For x>1 we have colloidal Regime I with overcrowded volume, stretched arms and $\Delta U_{hop} > k_BT$, while polymeric Regime II is linked to x<1. This single material parameter x can provide the needed design principle to tailor the dynamics of this class of soft materials across a wide range of applications from membranes for gas separation to energy storage.

INTRODUCTION

Grafting polymer chains onto a nanoparticle is a typical strategy to promote miscibility and homogeneity in nanocomposites.[1–5] Grafted nanoparticles (GNP) comprise a hard inorganic (hydrophilic) core and an organic (polymeric) shell; their surfactant-like structure makes them attractive as hybrid building blocks for hierarchical assemblies and new functional materials.[6] The presence of grafted chains prevents nanoparticle aggregation, although this strongly depends on the surface coverage. Interparticle interactions can be strongly affected and tuned by changing the degree of polymerization of the tethered chains, the grafting density, the grafting density distribution and the size of the core. Most often, GNPs are dispersed in a matrix of polymer chains or oligomers having the same chemistry as the grafted chains. Several theoretical, experimental and computational approaches have been used in the last 30 years to investigate the structural properties and dynamics of these systems.[3–14]

When GNPs or star polymers (which represent the limiting case of GNPs with a very small core) or ordered block copolymer spherical micelles are self-suspended in the melt state, i.e., in

solvent-free conditions, they interact in a completely different way in comparison to the case in which they are placed in a polymeric matrix or a molecular solvent.[3,15–28] This is the focus of the current work. In fact, GNPs with high enough grafting density and long enough grafted chains are well-dispersed and interact primarily via their coronas which can interpenetrate.[14] It was shown[4] that such suspensions exhibit multiscale structural transitions (e.g., the GNPs organize into crystalline lattices) and improved conformational stability as a result of strong steric repulsion between the grafted chains and space-filling constraints on the tethered chains in the single-component self-suspended material. Recently, it has also been shown that self-suspended GNPs are characterized by slow equilibration dynamics and structural evolution with time.[29] In fact, Archer *et al*.[29] determined, by using a combination of rheological and X-ray scattering measurements, that neat GNPs exhibit structural peaks which become enhanced over time, as a consequence of the significant equilibration process involving local rearrangements of the grafted chains. This feature was shown to be accompanied by an increase of the strength of the effective cage (which reflects the topological constraints of neighboring particles), as evidenced by the time evolution of the plateau storage modulus. Another study[20] reported the absence of terminal flow within the experimentally accessible time window. Such behavior was attributed to the coupling between arm interpenetration and particle localization (due to interparticle interactions); however, there was no explicit discussion of structural or jamming dynamics, i.e., the decoupling of polymeric and colloidal modes.

In this context, it is instructive to consider multiarm star polymer melts, which represent an important class of model self-suspended grafted nanoparticles (with zero core radius) which have been investigated extensively.[30–32] In particular, it was shown that melts of stars with a functionality f =64 or 128, and number of entanglements per arm between 4 and 43 exhibit a two-step stress relaxation, comprising a polymeric arm relaxation and a slow colloidal mode.[13,33] The latter was associated with the liquid-like ordering of the stars and attributed to a cooperative hopping process akin to cage escape in colloidal glasses.[33] Recently, experimental results with stars of very high functionality (f >850) and low arm size (2-3 entanglements) indicate a substantial dynamic arrest with dramatic slowing-down of the topologically constrained colloidal mode, which was assigned to colloidal jamming.[34] These findings call for a deeper understanding of the colloidal jamming transition in melts of hairy nanoparticles and question its potential universality

with a final ambitious goal to obtain the needed ingredients to describe jamming from hard spheres (point contacts, see also Figure S1 of the SI) to deformable impenetrable spheres (facets) to hairy spheres and to star polymers (interpenetration).

Recent simulations[8] have shown that the structural relaxation of self-suspended GNPs with long chains have higher relative diffusivities than their short chain counterparts, which may exhibit caging analogous to that of hard spheres. Depending on the GNP's internal microstructure, i.e., the number and size of grafted chains, the segments of the grafted chains near the particle surface can be stretched or effectively frozen. A point of crucial importance is the degree to which the coronas of densely grafted particles can interpenetrate. Theoretical analysis of polymer brushes in contact with chemically identical homopolymers shows that low molar mass homopolymers (free melt chains penetrate and swell the brush), whereas for high molar mass homopolymers this interpenetration and swelling occurs only partly.[35–37] For pure GNP melts with the same grafting density, increasing the size of the grafts should initially reduce the relative amount of interpenetration due to enhanced stretching of the inner section near the core.[33,35,36] However, further increases in the graft size would saturate the inner chain stretching and increase the interpenetration like in star polymers. Recent coarse-grained molecular dynamics simulations on GNP melts[38] demonstrated that the chain extension free energy is nonmonotonic as the molar mass of the grafted chains increases at a fixed grafting density. A maximum in free energy was detected, corresponding to the crossover from a dry layer-dominated to an interpenetration layer-dominated brush conformation regime.[38]

In the past few years, GNPs were proposed as promising candidates for gas separation membranes.[39–43] Membranes of self-suspended poly(methyl acrylate)-grafted silica nanoparticles exhibited elevated gas permeability with respect to the corresponding linear polymer chains.[43] The effectiveness of these membranes depended on the molar mass of the tethered chains in a non-monotonic way. This was linked to an increase in effective free volume, which was defined as the unoccupied (interstitial) volume, which in turn depended on the grafting density and the graft molar mass.[15,44] These interesting developments and related technological challenges necessitate the ability to tailor the properties of GNPs. Hence, they pose a fundamental question: how do the dynamics of self-suspended GNPs depend on their internal microstructure?

In the present work, we address the above challenge using a series of poly(methyl acrylate)-grafted silica nanoparticles (PMA- SiO_2), which essentially have a fixed grafting density but different degrees of polymerization (see Table M1) and multiarm polybutadiene stars of very high functionality and relatively small arm degree of polymerization (see Table M2). It was shown in previous investigations[15,30] that such model nanoparticles with a uniform grafting density are homogeneously distributed into a spatially amorphous structure. We quantitatively describe the polymeric and colloidal contributions to the dynamics of these soft colloids. We identify the threshold marking the transition from polymeric-dominated to colloidal-dominated response, and propose a generic dynamic diagram, where data from star polymers and GNPs are unified into a plot with regimes corresponding to different behaviors.

RESULTS AND DISCUSSION

Linear viscoelastic properties. Master curves of the storage moduli, loss factors, and shift factors for GNP samples 196k, 94k and 33k (we use for simplicity this nomenclature, see Table M1) are shown in panels A, B and C of Figure 1, respectively (full spectra are provided in Figure S2 in the SI). The master curves of the storage moduli G' (Figure 1A), are obtained from the time temperature superposition principle (tTS) (see Figure S3 of the SI for the validity of the tTS) and creep conversion (see Figures S4-S7); they cover nearly 16 decades in frequency, from the glassy regime to the structural relaxation of the system. The master curves are shown at the same temperature distance (40 °C) from the glass transition temperature (T_g), as an increase in silica content resulted in a slight T_g increase (see Table M1 and Figure S2 of the SI). Under these conditions, monomeric iso-friction conditions are guaranteed for comparison among particles with different degrees of polymerization (or silica contents). Moreover, we note that the combination of high grafting densities and topology, which is responsible for the "dry" and "wet" layer conformations of GNPs and stars, gives rise to regimes of distinct local mobility.[45–47] In the present work we focus on large-scale dynamics associated with the response of grafted arms and of the entire nanoparticle. The results indicate rich relaxation dynamics with both polymeric and colloidal contributions observable in the same rheological spectrum and occurring at different time (and length) scales. These spectra show qualitative resemblance with recent results obtained for star polymers of very high functionality.[34] With decreasing frequency, all the specimens show a glassy

regime (in high-frequency region for $\omega a_T > 10^5$ rad/s in Figure 1A) followed by a transition region and a polymeric plateau associated with arm entanglements. The latter is consistent with the behavior of pure PMA chains (about 0.25 MPa).[48] However, an increase in the plateau value is detected as the silica content in the samples increases (or the degree of polymerization of the tethered chains decreases). This filler reinforcement effect follows a Guth-Gold[49,50] trend with the silica volume fraction (see Figure S8 of the SI). The chain entanglement plateau extends on the frequency scale as the degree of polymerization of the grafted chains increases (see Figure 1A). This is reminiscent of the arm retraction relaxation mechanism[51] reported in several experimental studies on star polymers.[33,52] Indeed, if one imagines grafting significantly longer chains, so that the core becomes relatively small in size as compared with the polymer chains, the star-polymer limit should be reached, which is apparently the case for the 196k sample (green line), i.e., the linear viscoelastic modulus decreases with decreasing frequency until the terminal regime is reached, as expected.[52]

A more interesting behavior is observed when the grafted chains are shorter. Indeed, for $M_{arm} \leq 94$ kg/mol (with about 8.5 entanglements) we see an unambiguous additional mode characterized by a low-frequency plateau, which is about 100 times lower in comparison to the entanglement plateau, and an eventual relaxation which is about 1000 times slower than for the 196k sample. Despite the eventual terminal relaxation, we attribute this unusually slow time and low plateau modulus to a jammed colloidal material (i.e., with predominant solid-like character),[29,34] as discussed further below. It should be noted that soft colloidal glasses with an observable alpha relaxation have been discussed in the literature.[16–18,53,54] These findings suggest that upon reducing the arm molar mass, the polymer-dominated response is augmented by a hierarchical relaxation mechanism where arm retraction is followed by a colloidal relaxation process. Colloidal cage-escape[55,56] dynamics continue until structural relaxation of the system takes place, as proposed for multiarm star polymers.[33,34] It is important to note that the lowest four frequency decades are not accessible by means of the tTS, as the temperatures required to reach these frequencies in conventional small-amplitude oscillatory shear measurements are prohibitively high and the samples would degrade. To overcome this issue, creep experiments were performed and the measured compliances were converted into dynamic moduli (see Figures S4-S7 of the SI).[57–59]

Rheological spectra can also be analyzed using the loss factor ($\tan\delta = G''/G'$) as a function of frequency (Figure 1B). This representation facilitates the determination of the characteristic times of the materials, as the inverse frequency at the loss factor peaks or the moduli crossover ($\tan\delta=1$), as indicated by arrows in Figure 1B.[60,61] From high to low frequencies the following characteristic reciprocal frequencies (identifying relaxation times) are depicted in Figure 1B: the segmental relaxation time of a Kuhn monomer τ_0, the Rouse relaxation time of an entanglement strand τ_e, the arm retraction time τ_{arm} and the structural or terminal relaxation time τ_{term}. Note that τ_0 and τ_{arm} refer to relative maxima in $\tan\delta$, which imply maximum viscous dissipation in the system, while τ_e and τ_{term} are estimated as the inverse frequency at which $\tan\delta = 1$.[51,61] Whereas there is a clear distinction between τ_{arm} and τ_{term} for samples 94k and 33k, only one characteristic time, τ_{term}, is clearly observed for sample 196k (with about 18 entanglements), as the colloidal regime disappears and arm relaxation apparently becomes the terminal relaxation process. Moreover, τ_e and τ_0 are independent of the degree of polymerization of the chains (provided that the polymers are at least one entanglement long) and coincide for all the systems (see Table S1 of the SI). The frequency dependence of the loss factor can also serve to obtain the polymeric intermediate-frequency plateau modulus, $G_{plateau}$, and the colloidal low-frequency plateau modulus associated with entanglements, G_{LF}, as discussed below. These quantities coincide with the storage modulus at the angular frequency where the loss factor exhibits a relative minimum, in other words, where the elasticity of the system is the highest (see the arrows in Figure 1B). The characteristic times and plateau moduli are reported in Table S1 of the SI. Note also that for all the GNP melts studied we found uniform spatial organization of densely packed objects whose center-to-center distance scales with the total molar mass with a power-law exponent of 1/3 (see Figures S26-27 and X-ray scattering analysis section of the SI).

Horizontal (a_T) and vertical (b_T) shift factors are reported in Figure 1C along with those for pure PMA linear chains. The a_T values for the GNPs do not differ from the pure PMA chains and their temperature dependence is well-described by the Williams-Landel-Ferry (WLF) empirical equation[62] with constants $C_1 = 6.9$ and $C_2 = 93.2$ K at $T_{ref} = 60$ °C (neat PMA). This highlights an important finding, that despite of the existence of the colloidal mode, the dynamics are still controlled by the monomeric friction dependence on temperature. This may not be the case for lower grafting densities but this challenge goes beyond the scope of this work. The vertical shift

factors b_T only depend on the temperature variation of the PMA density and can be described by a polynomial function of the absolute temperature, as reported in the literature.[63] The density varies by less than about 20% over the range of temperatures investigated. One may argue that the experimental samples contain a large fraction of silica, hence, this should be also taken into account for the density variation. However, significant density variations for silica are only expected above 2000 K,[64] well above the temperature range probed in our experiments.

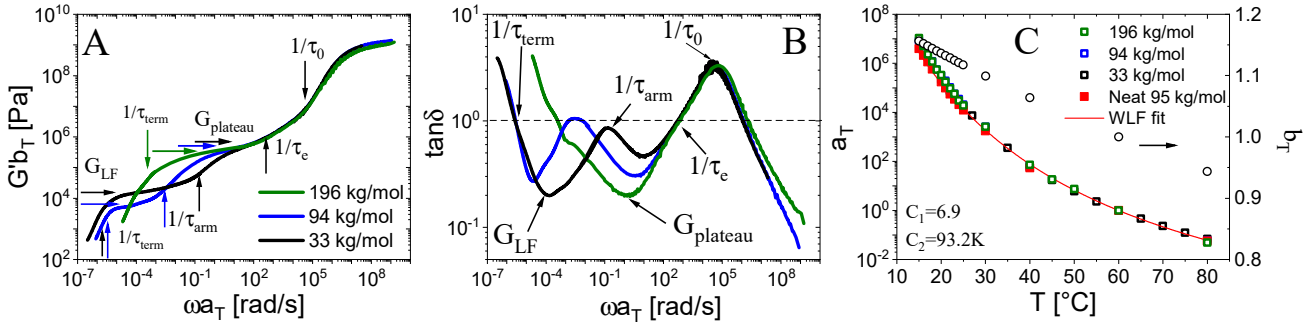

Figure 1. Linear viscoelastic master curves in terms of A) shifted storage modulus ($G'b_T$) and B) loss factor (tanδ) at the same relative temperature above T_g (T-T_g = 40 °C) as a function of the shifted oscillatory frequency (ωa_T). Panel C shows the corresponding horizontal (squares) and vertical (circles) shift factors. Black arrows in panels A and B mark the characteristic times (as inverse frequencies) and plateau moduli for the systems (see text), and the horizontal dashed line in panel B refers to equal storage and loss moduli ($G' = G''$, tanδ= 1). The red solid line in panel C represents the Williams-Landel-Ferry (WLF) fit whose constants are also reported in the graph for T_{ref} = 60 °C. The shift factors for neat PMA 95k are also reported as solid red squares.

Simple model for the dynamics of jammed GNPs. The main finding of this work is that the GNP melts undergo a viscoelastic liquid-to-jamming transition for grafted arm molar masses between 94k and 196k. It is important to emphasize that the experimental signatures of jamming are the presence of a low-frequency plateau modulus and an extremely slow or inaccessible terminal relaxation. To better understand this transition, as well as the tendency for the largest grafted arm 196k sample to behave akin to a star polymer melt, we examined separately the polymeric and colloidal contributions to stress relaxation. To this end, we followed a synergistic three-step approach consisting of (i) the analysis of arm relaxation through tube modeling (for entangled

arms), (ii) consideration of the structure of the grafted polymer layer with a region close to core where chains of neighboring particles cannot penetrate (dry layer), and an outer region where chain interdigitation occurs (wet layer), and (iii) analysis of the colloidal cage escape mode by invoking a hopping potential of the elastically deformed jammed particles.

First, we analyzed the polymeric response using the Milner-McLeish (MM) tube model for stars[33,65] accounting also for fast Rouse and longitudinal modes.[66,67] We identified the experimental polymeric relaxation time (Figure 1B, Table S1), and determined the fraction of the grafted arm s_{eff} that relaxes according to the MM model (i.e., the degree of interpenetration), by fitting the theoretical stress relaxation modulus $G(t)$ (which is a function of the size of the disentangling sections of arms) up to a characteristic size that corresponds to the experimental polymeric time. Even though this time represents only the relaxation of a fraction of the arm (s_{eff}), we call it τ_{arm} hereafter. The relaxation modulus $G(t)$ as per Milner-McLeish is given by

$$G(t) = G_{plateau}\left\{\frac{1}{Z}\sum_{p=Z}^{N_{arm}} exp\left(-\frac{2p^2t}{\tau_R}\right) + \frac{1}{5Z}\sum_{p=1}^{Z-1} exp\left(-\frac{2p^2t}{\tau_R}\right) + (x+1)\int_0^{s_{eff}} (1-s)^x exp\left[\frac{-t}{\tau_{arm}(s)}\right] ds\right\} \quad (1)$$

where the first two terms in the right-hand side of eq.1 represent the fast Rouse and the longitudinal modes, respectively, with τ_R being the Rouse time of the arm, estimated as $\tau_R=\tau_e Z^2$, and τ_e is the relaxation time of an entanglement strand containing N_e monomers, and $Z=N_{arm}/N_e$ is the number of entanglement strands per chain. The quantity $x = 4/3$ is the dilution exponent,[51,65,68] and $\tau_{arm}(s)$ is the arm relaxation time involving the early sub-diffusive and the late activated modes, as described by the MM model.[33,65] The upper limit of the integral s_{eff} is determined from the fit to the experimental data and provides a decent approximation of the fraction of the arm that has relaxed via arm retraction. This scenario is illustrated in the idealized schematic shown in Figure 2. The grafted chain can be divided into two sections: (i) an inner "dry" layer which is close to the nanoparticle core and is not interpenetrated by the chains of neighboring nanoparticles, and (ii) an outer layer, which is interpenetrated by chains from other GNPs and is called "interpenetrated or wet layer".[34–36,38] The former comprises a fraction (1-s_{eff}) of the grafted chain which we propose,

as a first approximation, to be associated with an average molar mass $M_{1\text{-}s_{eff}} = (1\text{-}s_{eff})\, M_{arm}$, and the latter corresponds to a chain fraction s_{eff} with a respective molar mass $M_{s_{eff}} = s_{eff}\, M_{arm}$. We emphasize that, while in our analysis we used the average molar mass of the interpenetrating arm, however, in reality, there is a distribution in each layer that may lead to a broader spectrum of arm retraction times; this has been treated rigorously in the literature.[33,69] We also ignored the fact that not all the arms are expected to enter the interpenetration zone. Depending on their internal microstructure (which is controlled by f and N_{arm}), there are GNPs exhibiting predominantly a jammed colloidal response (Regime I in Figure 2) and GNPs with a polymeric response (Regime

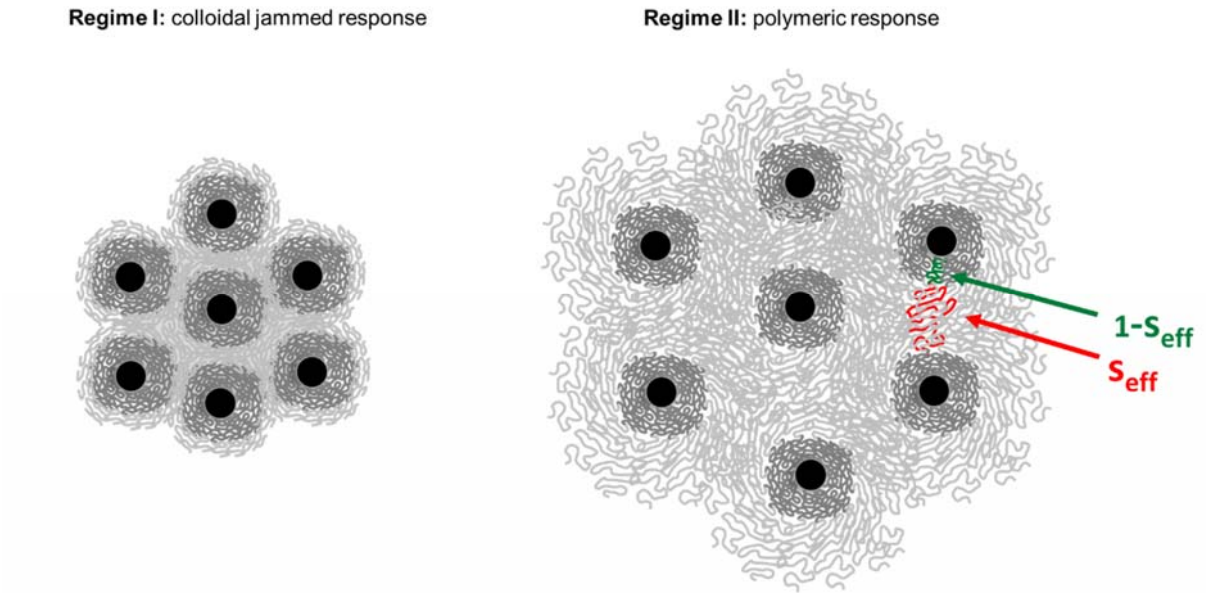

Figure 2. Schematic representation of GNP melts. Each GNP comprises a nanoparticle core (black), dry and wet layers (impenetrable to and interpenetrated by the arms of neighboring GNPs, respectively), the size of which depends on the grafting density (which is constant here) and the degree of polymerization of the grafted chains. The purposely marked dense (dark) near-core region represents the dry layer (green portion of the colored arm in Regime II), while the interstitial area is the interpenetrated (or wet) layer region (red portion of the arm in Regime II). These two regions correspond to arm fractions $(1\text{-}s_{eff})$ and s_{eff}, respectively, in eq. 1 (see text). In Regime I, the terminal relaxation (if attainable) is dominated by a colloidal-jammed response, and in Regime II by polymeric arm relaxation. The crossover from Regime I to Regime II is broad (see text).

II in Figure 2). It should be noted that application of the MM tube model to highly grafted brushes with a low M_{arm}, Z <5, is not rigorous,[34] and hence we mainly restrict our discussion to brushes with Z > 5. The transition from the "predominantly colloidal" Regime I, where the GNP melts exhibit jammed colloidal response akin to caged particles,[34] to "predominantly polymeric" Regime II, where relaxation of the mutually interpenetrated grafted arms controls the GNP response, is not sharp. Instead, there is an intermediate situation without clear colloidal plateau, with arm retraction and colloidal relaxation modes close to each other, albeit distinct, corresponding to a colloidal hopping potential (discussed below) exceeding thermal energy and well-entangled arms (see Figures 8 and S2, S16, and S17 of the SI).

Typical MM fitting results (eq. 1) are presented in Figure 3 for two cases: a polymeric-arm dominated Regime II (for the highest arm molar mass studied, 196k) and a situation where both polymeric and colloidal responses are clearly discerned (for M_{arm}=94kg/mol). This figure depicts the dynamic moduli, after converting the stress relaxation modulus of eq. 1,[60] and the resulting effective degree of polymerization of the interpenetrated sections of arms (s_{eff}) determined from these fits is listed in the legend. The fits to the MM model for the other arm molar masses are reported in Figures S15-S20 of the SI. GNPs with long arms, i.e., $M_{arm} > 94$ kg/mol, are not jammed (the potential barrier for colloidal hopping discussed below is lower than k_BT and Z>>1) and relax similarly to star polymers (Regime II in Figure 2), while GNPs with shorter arms ($M_{arm} \leq 94$ kg/mol) exhibit a response akin to soft colloidal jamming (Regime I in Figure 2). The results of the MM fits in terms of arm relaxation time and interpenetrated Kuhn degree of polymerization (corresponding to fraction s_{eff}, of the grafted arm in Figure 2) are reported in Table S3 of the SI. A more rigorous determination of the degree of polymerization of the interpenetrated layer, N_{inter}, is based on the use of a brush conformation model and is presented in the SI (Figures S12 and S13A). Once the average N_{inter} in each layer is known, the respective thickness can be estimated from the brush conformation model (Figure S13B). In this context, the fraction of dry (non-interpenetrated arm) material, expressed as the ratio M_{dry}/M_{arm}, was also determined and is displayed in Figure S14. This quantity is inherent in the overcrowding parameter, x, which is the ratio of number of grafted arms f to the maximum number of unperturbed chains with N_{arm} that can fill the volume occupied by the polymeric corona (see SI and Ref. 38). We show below that

this single parameter determines the predominantly polymer or colloidal response in the GNPs and other hairy nanoparticles.

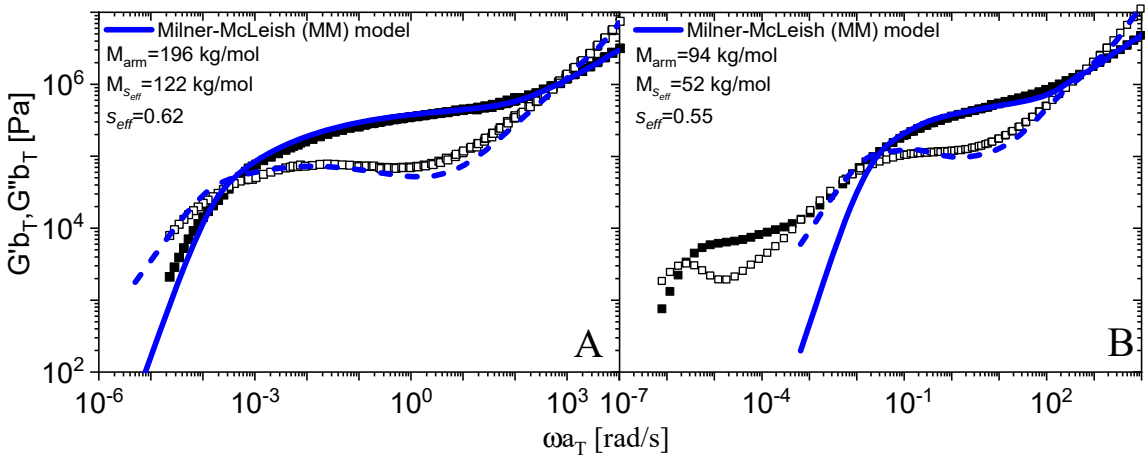

Figure 3. Linear viscoelastic master curves in terms of shifted storage ($G'b_T$) and loss ($G''b_T$) moduli as a function of the shifted oscillatory frequency (ωa_T) at 40 °C above the glass transition temperature (T-T_g = 40 °C) for the GNP samples 196k (Panel A) and 94k (Panel B). The solid and dashed blue lines represent the storage and loss moduli obtained from the MM model, respectively. M_{arm} is the total arm molar mass, s_{eff} is the fraction of the arm in the interpenetration layer, corresponding to a molar mass M_{seff}.

We now analyze the slow colloidal response of the GNPs and in particular those belonging to the jamming Regime I. In this case, after relaxation of their arms, the GNPs remain jammed, i.e., trapped into effective cages and attempt to escape them by hopping. To undergo hopping between neighboring cages, a GNP needs to overcome a free energy barrier ΔU_{hop}.[33,34,70–72] The cage escape process is characterized by a terminal relaxation time

$$\tau_{term} \approx \tau_{attempt} exp\left[\frac{\Delta U_{hop}}{k_B T}\right] \quad (2)$$

where the attempt time $\tau_{attempt}$ is estimated following the analysis of Kapnistos *et al.*[33] We suggest that the cage escape of GNPs with respect to their neighbors requires disengagement/re-engagement of the arms and hopping. The friction coefficient of a GNP is proportional to the number of arms, f = 378 times the effective friction per arm ~ $k_B T \tau_{arm}/(\Delta R)^2$. We estimated the displacement of the interpenetrated section of an arm during retraction (over the time scale τ_{arm}) by the thickness of the interpenetrated zone (red section in Fig. 2), $\Delta R \approx b N_{inter}^{1/2}$, considered to be Gaussian,[33,38] with b= 1.47 nm being the Kuhn monomer length.[48] The corresponding displacement of the entire GNP due to single arm retraction is $\frac{\Delta R}{f}$. The mean square displacement for such a single event is $\frac{(\Delta R)^2}{f^2}$, while there are f such events during the time interval τ_{arm}. This yields an "attempt" diffusion coefficient for the GNP within a cage:

$$D_{attempt} \approx f \frac{(\Delta R)^2}{\tau_{arm} f^2} \qquad (3)$$

The hopping step has a very low probability in this crowded environment, and hence many attempts are needed for a jammed GNP to escape from its effective cage. The respective attempt time is on the order of the diffusion time of the GNP over a distance comparable to its total radius R in the absence of potential barrier, where the total radius of the GNP is

$$R = \left[\left(R_{core}^3 + \frac{3}{4\pi} v_0 f N_{arm}\right)\right]^{1/3} \qquad (4)$$

R_{core} = 8 nm is the average (volume averaged) radius of the silica core, N_{arm} is the Kuhn degree of polymerization of the graft with a molar mass M_{arm}, $v_0 = \frac{M_0}{N_A \rho}$ is the volume of the Kuhn monomer (v_0 = 0.673 nm^3 for a Kuhn molar mass M_0 = 494.6 g/mol[48] and ρ = 1.22 g/cm^3 [63]). The total particle radius calculated from eq. 4 is in good agreement with the characteristic length extracted from X-ray measurements (see Figures S26 and S27 of the SI).

The attempt time is therefore proportional to the square of the diffusion distance R^2 divided by the attempt diffusion coefficient $D_{attempt}$ (eq. 3), which yields:

$$\tau_{\text{attempt}} \sim \frac{R^2}{D_{attempt}} = a\tau_{\text{arm}} f \frac{R^2}{(\Delta R)^2} \quad (5)$$

where *a* is a coefficient determined from the best fit of the experimental terminal relaxation times as discussed below; it is found to be equal to 2. The arm relaxation time τ_{arm} in eq. 5 can be estimated either by using the experimental value (Figure 1 and Table S1) or with the MM model, using N_{inter} extracted from the two-layer brush conformation model (see Table S4 of the SI and Figure 8 below).[38] The GNPs with the largest M_{arm} > 130 kg/mol are excluded from this analysis, as in the absence of a colloidal barrier the stress is mainly relaxed by τ_{arm}. Indeed, as already mentioned, this M_{arm} marks a threshold, beyond which (for longer arms) the terminal relaxation of a GNP is dominated by arm retraction (the dry zone fraction is small enough for the GNPs to diffuse past each other without the barrier, see Figures S13, S14 and Table S5 of the SI).

The hopping potential ΔU_{hop} represents the barrier for cage escape of the GNP with a certain attempt time, and is approximated below by means of a simple scaling analysis, which is based on the compression of a GNP by its neighboring GNPs during its hopping step. Let us consider such a caged GNP in Figure 4 and assume, for simplicity, that it forms three facets during the transition state of the hopping process between neighboring cages. The overall GNP deformation γ_{GNP} is its fractional compression, i.e., $\gamma_{GNP} = 1 - \frac{D}{R}$, where *D* represents the size the deformed particle (of initial radius *R*) as depicted in Figure 4 (estimated values are reported in Table S6 of the SI). The hopping potential is the change in elastic energy of the GNP due to extension of its arms (from initial length h_{pol} to h'_{pol}) because of the creation of the facets (see Figure 4). It is proportional to the change in respective elastic energy per arm, $\frac{{h'_{pol}}^2}{b^2 N_{arm}} - \frac{{h_{pol}}^2}{b^2 N_{arm}}$ (see also Figure S21 of the SI). In addition, we need to account for the number of chains per facet as well as the number of facets (three for the examined GNP and one for each of its three neighbors in the cage, i.e., a total of six facets, see Figure 4). We combined all these coefficients into a single parameter A times the number of arms *f* and expressed the activated hopping model potential as

$$\Delta U_{hop} = \mathrm{A} f \left(\frac{{h_{pol}}^2}{b^2 N_{arm}} - \frac{{h'_{pol}}^2}{b^2 N_{arm}} \right) k_B T \quad (6)$$

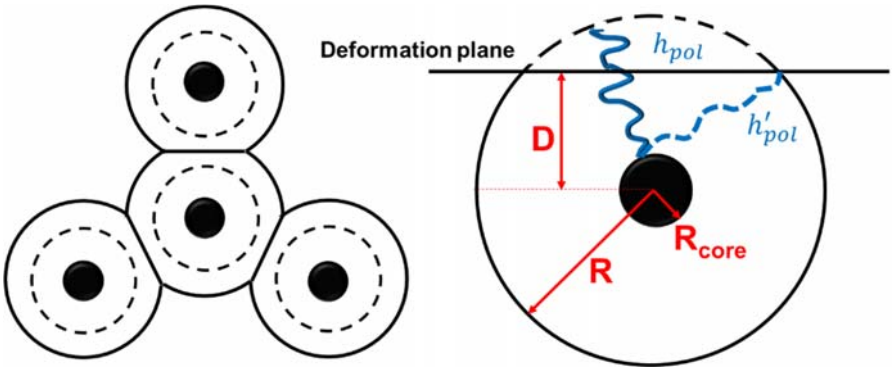

Figure 4. Schematic representation of deformed particles forming facets (left side), and arm stretching events during particle deformation (right side). D is the depth of the deformation plane, and h_{pol} and h'_{pol} are, respectively, the length of the chains prior to and after deformation sets in.

The explicit form of the hopping barrier height is

$$\Delta U_{hop} = Af\left(\frac{R^2 - D^2 + (D - R_{core})^2}{b^2 N_{arm}} - \frac{(R - R_{core})^2}{b^2 N_{arm}}\right) k_B T \tag{7}$$

Using the expression for the GNP radius R (eq. 4) we can estimate the free energy barrier

$$\frac{\Delta U_{hop}}{k_B T} = B\left(\frac{f}{(R_{core}^3/v_0)^{1/4}}\right)^{4/3}\left(\frac{R_{core}^3}{v_0 f N_{arm}}\right)^{2/3}\left(1 + \frac{R_{core}^3}{v_0 f N_{arm}}\right)^{1/3} \tag{8}$$

where the coefficient $B = 2A\left(\frac{3v_0}{4\pi b^3}\right)^{\frac{2}{3}}\left(1 - \frac{D}{R}\right)$.

Dynamic state diagram. The condition $\Delta U_{hop} = k_B T$ which marks the transition from polymeric response without barrier to colloidal response, corresponds to

$$\frac{f}{(R_{core}^3/v_0)^{1/4}} = B^{-3/4}\left(\frac{N_{arm} v_0 f}{R_{core}^3}\right)^{1/2}\left(1 + \frac{R_{core}^3}{v_0 f N_{arm}}\right)^{-1/4} \tag{9}$$

Since $\frac{R_{core}^3}{v_0 f N_{arm}} \ll 1$ in the GNPs and stars (for systems investigated this ratio is ≤0.033), we can simplify the above equation and obtain a simple approximation for the boundary separating Regimes I and II:

$$\frac{f}{(R_{core}^3/v_0)^{1/4}} = B^{-3/4}\left(\frac{N_{arm}v_0 f}{R_{core}^3}\right)^{1/2} \quad (10)$$

In Figure 5 we plot experimental data of the normalized number of arms $\frac{f}{(R_{core}^3/v_0)^{1/4}}$ as a function of the normalized arm size $\frac{N_{arm}v_0 f}{R_{core}^3}$ for various experimental GNPs and stars which have been identified to exhibit polymeric (filled symbols, Regime II) or jammed colloidal (open symbols, Regime I) behaviors, while some (noted by X) exhibit a second weak relaxation mode without a well-discerned low-frequency plateau (extending over at least one decade); it this situation, ΔU_{hop} may slightly exceed $k_B T$ and Z>>1 (in fact, it is $Z_{s,eff}=M_{s,eff}/M_e$ >>1, see Figure 3 and SI). The line separating the polymeric and colloidal responses (Regimes II and I, respectively) is the above eq.10 with a value of the fit parameter B=0.1. This result is very satisfactory and appears to be universal. Details about the investigated multiarm star polybutadienes (1,4-microstructure) with very high branching functionalities (ranging from 875 to 2828, see Table M2), which exhibited colloidal jamming response, are provided in Figures S23-S25, and S27 of the SI.

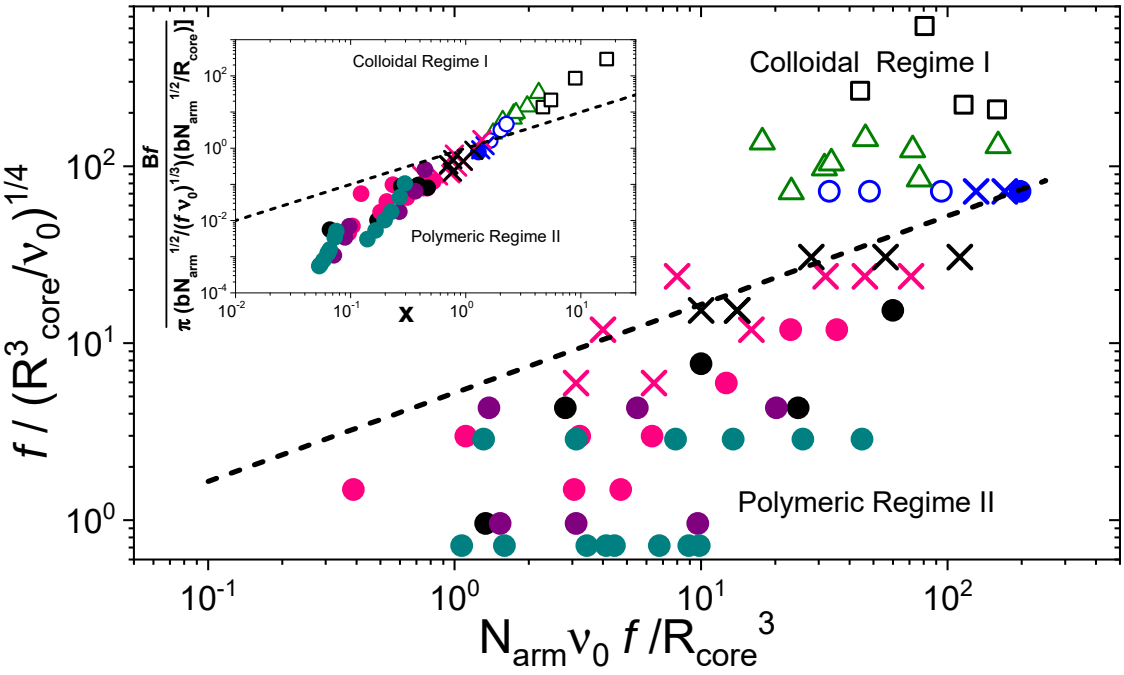

Figure 5. Dynamic state diagram for GNPs and stars in terms of $\frac{f}{(R^3_{core}/\nu_0)^{1/4}}$ against $\frac{N_{arm}\nu_0 f}{R^3_{core}}$ (see text). The filled circles represent systems whose dynamics are controlled by polymeric arm relaxation, cross symbols (X) refer to systems exhibiting hybrid (both polymeric and colloidal) response; in this case, the potential barrier for hopping exceeds k_BT and $Z_{s,eff}$>>1, and open symbols refer to the jammed colloidal regime where an extended low-frequency colloidal mode (with a long relaxation time, if reached, as compared with the arm time) dominates the rheological spectrum. The blue symbols represent the present GNPs. The open green triangles are PEO GNPs from Refs.16,29, and black squares refer to star polymers investigated here (Figures S23-S25) and partially in Ref. 34. The black crosses and circles are star polymers from the literature.[30,33,73] Polyisoprene (PI) stars with low functionalities f = 3 and f = 12, and f = 4 and f = 18, taken from the literature, are displayed as filled dark cyan[74] and filled purple circles,[75] respectively. Polystyrene stars with a branching functionality in the range 2-64, taken from the literature,[76] are displayed as magenta filled circles and crosses. Dashed line is Eq. 10 and dotted line is eq.9. Inset: Alternative double logarithmic representation of the main plot with the experimental data being plotted as the normalized functionality of the hairy nanoparticles versus overlap parameter x. The dashed line is eq.11with B=0.1.

To justify the values of the parameters *A* and *B*, we consider that the average deformation $\gamma_{GNP} = 1 - \frac{D}{R}$ is in the range 0.1 to 0.3. The respective surface of the spherical cap deformed by γ_{GNP} is *2πR(R-D)* and occupies a fraction of the total GNP surface of $\frac{2\pi R(R-D)}{4\pi R^2} = \frac{\gamma_{GNP}}{2} = 0.05 - 0.15$. The number of chains per facet is $\frac{\gamma_{GNP}}{2} f$. For a total of six facets, this leads to A = $\frac{2\pi R(R-D)}{4\pi R^2} 6 = 3\gamma_{GNP}$ ≈ 0.3 - 0.9. Note that a number of simplifications/assumptions were used: The degree of interpenetration per arm was considered to be the same, the number of facets was assumed to be 3x2=6, and the deformation per arm was considered to be the same. Since the parameter $\left(\frac{3v_0}{4\pi b^3}\right)^{2/3}$ for different chemistries does not vary substantially (see also SI), we assigned an average value of 0.15 to this parameter. This yields values of B ranging from 0.03 to 0.09, which is close to the value 0.1 selected above. As a consistency check, we compared the potential from eq. 8 with the potential extracted from eqs. 2 and 5 using experimental data for terminal and arm times, and found that the agreement was reasonable (see Figure S22 and Table S7 of the SI).

Using the definition of the overcrowding parameter $x = \frac{f}{\frac{\pi b^2}{v_0}\left(R_{core}^3 + \frac{3fN_{arm}v_0}{4\pi}\right)^{1/3}}$ (see also SI and Ref.33) and eq.9, we can re-write eq.8 as

$$x = \frac{B\,f}{\pi\left(\frac{bN_{arm}^{1/2}}{(fv_0)^{1/3}}\right)\left(\frac{bN_{arm}^{1/2}}{R_{core}}\right)} \qquad (11)$$

This equation reflects the condition $\Delta U_{hop}=k_BT$, expressed in terms of *x*, with the right-hand side representing a normalized functionality of the hairy nanoparticle. The inset of Figure 5 plots the same experimental data in terms of this normalized functionality versus *x*. The data virtually collapse onto a power-law line with exponent of about 7/3. The dashed line is eq.11 with B=0.1 and crosses that data at the point (1,1), which marks the universal transition from colloidal response (Regime I) for *x>1* to polymeric (Regime II) for *x<1*. Hence, *x* is the single material parameter to design such systems with desired colloidal vs polymeric response.

Plateau modulus and cage escape. With the hopping potential being able to describe reasonably the free energy barrier for a GNP to escape from its colloidal cage, as judged from the dynamic diagram of Figure 5, we now use eq.8 to determine the colloidal plateau modulus, which is the hopping barrier per particle volume, $G_{LF} = \frac{\Delta U_{hop}}{R^3}$, and normalize it by the thermal energy per particle volume:

$$\frac{G_{LF}R^3}{k_BT} = CB\left(\frac{f}{(R_{core}^3/v_0)^{1/4}}\right)^{4/3}\left(\frac{R_{core}^3}{v_0 f N_{arm}}\right)^{2/3}\left(1+\frac{R_{core}^3}{v_0 f N_{arm}}\right)^{1/3} \quad (12)$$

In this equation C is a prefactor which we determine below, while B=0.1 as alredy explained. Reorganization of eq.12 at the transition state where $\Delta U_{hop} = k_BT$ (i.e. by combining with eq. 11) yields

$$\frac{G_{LF}R^3}{k_BT} \approx C \quad (13)$$

We plot in Figure 6 the experimental $\frac{G_{LF}R^3}{k_BT}$ as a function of the overcrowding parameter x. As expected, the normalized modulus is defined only for $x \geq 1$ and increases with x. Extrapolation to x=1 yields $\frac{G_{LF}R^3}{k_BT} = 5$, which is the above extracted value of C, consistent with eq.13. Using C=5 we can determine the normalized low-frequency modulus from the right-hand side above of eq.12, which is in very good agreement with the experimental data for both GNPs and stars (see Table S8 of the SI).

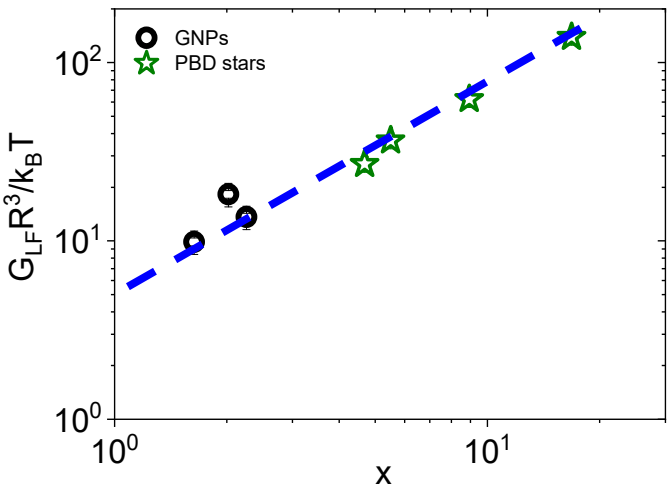

Figure 6. Experimental normalized low-frequency colloidal plateau modulus as a function of the overcrowding parameter for the GNPs and star PBDs investigated here. The blue dashed line through the data hits the ordinate at a value $\frac{G_{LF}R^3}{k_BT} = 5$.

The terminal time τ_{term}, calculated from eqs. 2,5 and 8 (using a = 2 and B=0.1) and extracted from the experimental data, is presented in Figure 7 where the different relaxation times are plotted as a function of $Z = N_{arm}/N_e$ (see also Table S7). The agreement of this simple model with the experimental data is quite satisfactory, with a notable deviation for the 130k sample (N_{arm}=263, Z≈12). This is expected, as the potential is larger in the jammed regime with large differences between the terminal and arm relaxation times (and large ΔU_{hop}), whereas in the polymeric high-Z regime there is no attempt process (see Figure 3 and Figures S15-S20 of the SI) and the MM model works satisfactorily. The terminal relaxation time is nearly constant for Z < 10 (while the arm relaxation time increases), and much larger than the arm relaxation time (up to 5 decades), while it decreases for larger Z values, eventually approaching the arm relaxation time. The open red and blue circles in Figure 7 represent the τ_{arm} estimated from the MM best fit to the experimental data (as outlined above) and the MM model prediction based on the relaxation of arm segments with a degree of polymerization N_{inter} calculated with the two-layer model, respectively (see Figures S15-S20 of the SI). The deviations suggest there are still subtle details in both the two-layer model and the MM analysis of arm relaxation in densely grafted nanoparticles and require further consideration in the future. However, they do not affect the emerging clear picture of transition from polymeric to colloidal dynamics at x=1 (at about Z≈12 for the present GNPs) as presented in Figure 5. Note that N_{inter} and N_{seff} deviate as Z increases (see Figure S13), and the associated arm relaxation times extracted from the two-layer and MM models differ. We attribute this, in part, to the approximate formulation of the partial arm retraction model in eq.1, as well as the fact that the two-layer model is essentially applicable for x≥1 (since for x<<1 it considers that arms overlap only with nearest neighbors), but more work will be needed to properly address this point. Another important point is the fact that a sizeable core would induce a steric repulsive constraint (retardation) on the arm retraction process, which is not accounted for here.[77,78] The ratio R_c / $\langle R^2 \rangle^{1/2}$ is small in the studied experimental nanoparticles (it varies from 0.27 to

0.48 for GNPs and 0.29 to 0.44 for stars) but not negligible, hence its role on arm retraction should also be addressed in the future (along with possible chain stretching near the core). In this context, we recall that the largest discrepancies in the values of N_{inter} extracted from the MM fit were observed for the largest values of R_c / $<R^2>^{1/2}$. We emphasize that these considerations could lead to improvements in the quantitative description of the dynamics, which however do not influence the message of the present work. Also depicted in Figure 7 are the predicted τ_{term} (open inverted triangles), from eq.2, and attempt $\tau_{attempt}$ (asterisks), from eq.5, times which are discussed below in the context of the slow mode analysis. The remarkable structural change experienced by the GNPs with increasing N_{arm} is also reflected in the dependence of their zero-shear rate viscosity on M_{arm} (see Figure S11 of the SI).

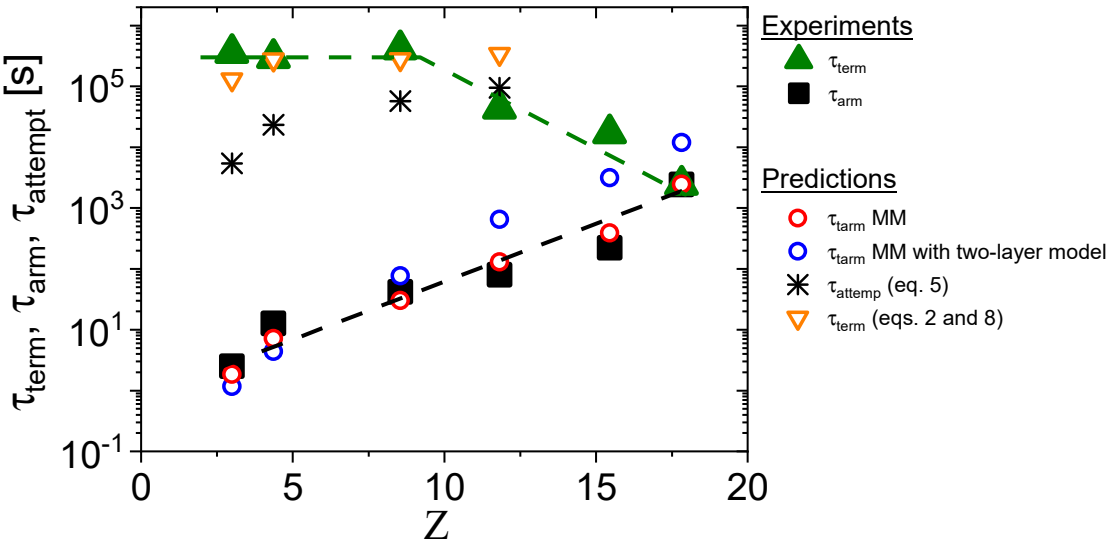

Figure 7. Experimental terminal (green filled up triangles) and arm relaxation (black filled squares) times for the GNPs, obtained from tanδ (Figure 1), as a function of Z, the number of entanglements per grafted arm. The circles, open down triangles and asterisks represent the model predictions for the arm, attempt and terminal relaxation times (see text), respectively. The dashed lines are drawn through experimental points to guide the eye.

CONCLUSIONS

We have shown how to decouple the dynamics of self-suspended hairy particles (grafted nanoparticles and star polymers in the melt state) into polymeric and colloidal contributions, and at the same time, their dynamics can be tailored from polymeric (viscoelastic liquid) to jammed colloidal, by varying the size of the grafted chain at fixed grafting density and core size. The former can be described quantitatively by a tube-based arm relaxation model and the latter by invoking a simple hopping model based on the elastic deformation of the caged particles. A transition from polymeric to jammed colloidal response is observed when the hopping potential becomes ~k_BT. which is shown to correspond to a value of the overcrowding parameter x=1. Hence, this structural parameter is now linked to the energetic barrier for hopping. Further, this allows constructing a universal dynamic state diagram in terms of normalized number of arms $\frac{f}{(R_{core}^3/v_0)^{1/4}}$ as a function of their normalized size $\frac{N_{arm}v_0 f}{R_{core}^3}$, applicable to a wide range of self-suspended hairy nanoparticles. Despite its simplicity our approach is robust and represents a first-order guide for the cross-over between colloidal and polymeric regimes in this class of materials, which is controlled by a single materials property, the overlapping parameter x. There are still many open questions such as how variations in chain extension in the dry zone can modify the arm retraction model, or how to make the hopping potential model more realistic by better estimating the number of facets, the number of arms in the interpenetration zone and the degree of interpenetration per arm.

Experimental Details

Materials and Methods

Grafted nanoparticles: Poly(methylacrylate) (PMA)-grafted silica (SiO_2) nanoparticles (16±4 nm core diameter, 0.47±0.4 chains/nm^2 grafting density) were synthesized by the surface-initiated reversible addition-fragmentation chain transfer polymerization (SI-RAFT) technique.[1,79] Details on the synthetic process and the reaction mechanisms can be found elsewhere.[80] The molecular characteristics of the investigated systems are reported in Table M1. The entanglement molar mass

of PMA is 11 kg/mol. Details on differential scanning calorimetry measurements and thermal gravimetric analysis (TGA) are described in Ref. 80. Small angle X-ray scattering results are shown in Figure S26 of the SI. The samples were all studied in the molten state. To mold the samples, approximately 65-75 mg of material was loaded into an 8 mm diameter stainless steel vacuum mold to yield disks of approximately 800-1000 μm thickness. Vacuum was applied inside the mold by connecting a hose on the chamber to the inlet of an air compressor. The mold was heated to 80 °C for 20 minutes and then allowed to cool gradually to room temperature, while maintained under vacuum. Depending on the experiment, 4 mm and 2 mm disks were also used.

Table M1. Molecular characteristics of silica-grafted nanoparticles.

Sample code	$M_{w,arm}$ [kg/mol]	Polydispersity of arms	ϕ_{core} (SiO_2 only)	ϕ_{core} (SAXS)	ϕ_{core} (TGA)	T_g [°C]
196k	196	1.3	0.021		unavailable	
170k	170	1.29	0.024	0.036	0.031	18.1
130k	130	1.28	0.031	0.051	0.043	unavailable
94k	94	1.2	0.043	0.07	unavailable	18
48k	48	1.16	0.081	0.139	0.12	18.1
33k	33	1.14	0.112	0.176	0.16	18.3

Multiarm star polymers: Polybutadiene (1,4 microstructure) stars, synthesized and characterized as described by Gauthier and Munam,[81] were used for additional data (see Table M2 for the molecular characteristics). The new stars used here have the following characteristics (based on chemical characterization)[81]: $f = 1114$, $M_{arm} = 1270$ g/mol and $f = 2828$, $M_{arm} = 1300$ g/mol, with polydispersity below 1.1, see Table M2. Small angle X-ray scattering results for some stars are reported in Figure S27 of the SI. Specimens for rheological tests were press-molded under vacuum into 4 mm disks.

Table M2. Molecular characteristics of multi-arm star polymers.

f	M_{arm} [kg/mol]	Polydispersity linear chains
875	5.8	1.08
929	4.0	1.03
1114	1.27	1.07
2828	1.3	1.10

Small Amplitude Oscillatory Shear and Creep measurements: Oscillatory shear experiments were conducted on an ARES stress-controlled rheometer using either an 8, 4 or 2 mm parallel plate geometry. The temperature was controlled by a convection oven fed with nitrogen gas to minimize sample degradation. Creep experiments were performed on an Anton Paar MCR702 instrument equipped with 8 mm parallel plates. After loading, typically at 80 °C, the samples were allowed to equilibrate for at least 30 minutes. Strain sweep experiments were carried out to determine their linear viscoelastic regime at each temperature. Dynamic time sweep experiments in the linear regime were also performed to ensure steady-state and thermal equilibrium conditions. Frequency sweeps were conducted from 100 – 0.1 rad/s at 5 °C intervals from 80 °C to 30 °C and at 2-3°C intervals between 27°C to 18°C (the latter corresponds to the glass transition temperature). Small amplitude oscillatory shear experiments for stars were performed in an ARES stress-controlled rheometer using a 4 mm parallel plate geometry in the temperature range -80 to 30 °C. The temperature was controlled with a convection oven connected to a liquid nitrogen Dewar container.

Acknowledgments

Partial support by the EU (ETN-COLLDENSE, H2020-MCSA-ITN-2014, Grant No. 642774) and the Greek Secretariat for Research and Technology (INNOVATION program-AENAO) is gratefully acknowledged. MR acknowledges financial support from National Science Foundation under Grant EFMA-1830957 and the National Institutes of Health under Grant P01-HL108808. SK acknowledges financial support for this research from the Department of Energy under grant DE-SC0021272. We thank Mayank Jhalaria for help in sample preparation and for many deep discussions on the topic of this paper.

Supporting Information

Conceptualization of topological jamming; Linear viscoelastic measurements and analysis; A simple brush conformation model; Modeling of polymeric arm relaxation; Slow mode analysis; Linear viscoelastic master curves of multiarm star polymer melts; X-ray scattering analysis.

References

(1) Li, C.; Han, J.; Ryu, C. Y.; Benicewicz, B. C. A Versatile Method to Prepare RAFT Agent Anchored Substrates and the Preparation of PMMA Grafted Nanoparticles. *Macromolecules* **2006**, *39* (9), 3175–3183.

(2) Chevigny, C.; Dalmas, F.; Di Cola, E.; Gigmes, D.; Bertin, D.; Boué, F.; Jestin, J. Polymer-Grafted-Nanoparticles Nanocomposites: Dispersion, Grafted Chain Conformation, and Rheological Behavior. *Macromolecules* **2010**, *44* (1), 122–133.

(3) Kumar, S. K.; Jouault, N.; Benicewicz, B.; Neely, T. Nanocomposites with Polymer Grafted Nanoparticles. *Macromolecules* **2013**, *46* (9), 3199–3214.

(4) Mangal, R.; Srivastava, S.; Archer, L. A. Phase Stability and Dynamics of Entangled Polymer–Nanoparticle Composites. *Nature Communications* **2015**, *6*, 7198.

(5) Alkhodairi, H.; Russell, S. T.; Pribyl, J.; Benicewicz, B. C.; Kumar, S. K. Compatibilizing Immiscible Polymer Blends with Sparsely Grafted Nanoparticles. *Macromolecules* **2020,** *53* (23), 10330-10338.

(6) Hore, M. J. Polymers on Nanoparticles: Structure & Dynamics. *Soft Matter* **2019**, *15* (6), 1120–1134.

(7) Meng, D.; Kumar, S. K.; Lane, J. M. D.; Grest, G. S. Effective Interactions between Grafted Nanoparticles in a Polymer Matrix. *Soft Matter* **2012**, *8* (18), 5002–5010.

(8) Chremos, A.; Panagiotopoulos, A. Z.; Koch, D. L. Dynamics of Solvent-Free Grafted Nanoparticles. *The Journal of Chemical Physics* **2012**, *136* (4), 044902.

(9) Sunday, D.; Ilavsky, J.; Green, D. L. A Phase Diagram for Polymer-Grafted Nanoparticles in Homopolymer Matrices. *Macromolecules* **2012**, *45* (9), 4007–4011.

(10) Moll, J. F.; Akcora, P.; Rungta, A.; Gong, S.; Colby, R. H.; Benicewicz, B. C.; Kumar, S. K. Mechanical Reinforcement in Polymer Melts Filled with Polymer Grafted Nanoparticles. *Macromolecules* **2011**, *44* (18), 7473–7477.

(11) Srivastava, S.; Agarwal, P.; Archer, L. A. Tethered Nanoparticle–Polymer Composites: Phase Stability and Curvature. *Langmuir* **2012**, *28* (15), 6276–6281.

(12) Lin, C.-C.; Griffin, P. J.; Chao, H.; Hore, M. J.; Ohno, K.; Clarke, N.; Riggleman, R. A.; Winey, K. I.; Composto, R. J. Grafted Polymer Chains Suppress Nanoparticle Diffusion in Athermal Polymer Melts. *The Journal of Chemical Physics* **2017**, *146* (20), 203332.

(13) Pakula, T. Static and Dynamic Properties of Computer Simulated Melts of Multiarm Polymer Stars. *Computational and Theoretical Polymer Science* **1998**, *8* (1–2), 21–30.

(14) Chremos, A.; Panagiotopoulos, A. Z. Structural Transitions of Solvent-Free Oligomer-Grafted Nanoparticles. *Physical Review Letters* **2011**, *107* (10), 105503.

(15) Bilchak, C. R.; Buenning, E.; Asai, M.; Zhang, K.; Durning, C. J.; Kumar, S. K.; Huang, Y.; Benicewicz, B. C.; Gidley, D. W.; Cheng, S. Polymer-Grafted Nanoparticle Membranes with Controllable Free Volume. *Macromolecules* **2017**, *50* (18), 7111–7120.

(16) Agarwal, P.; Qi, H.; Archer, L. A. The Ages in a Self-Suspended Nanoparticle Liquid. *Nano letters* **2009**, *10* (1), 111–115.

(17) Choudhury, S.; Agrawal, A.; Kim, S. A.; Archer, L. A. Self-Suspended Suspensions of Covalently Grafted Hairy Nanoparticles. *Langmuir* **2015**, *31* (10), 3222–3231.

(18) Srivastava, S.; Choudhury, S.; Agrawal, A.; Archer, L. A. Self-Suspended Polymer Grafted Nanoparticles. *Current Opinion in Chemical Engineering* **2017**, *16*, 92–101.

(19) Choi, J.; Hore, M. J.; Clarke, N.; Winey, K. I.; Composto, R. J. Nanoparticle Brush Architecture Controls Polymer Diffusion in Nanocomposites. *Macromolecules* **2014**, *47* (7), 2404–2410.

(20) Sakib, N.; Koh, Y. P.; Huang, Y.; Mongcopa, K. I. S.; Le, A. N.; Benicewicz, B. C.; Krishnamoorti, R.; Simon, S. L. Thermal and Rheological Analysis of Polystyrene-Grafted Silica Nanocomposites. *Macromolecules* **2020**, *53* (6), 2123-2135.

(21) Gohr, K.; Pakula, T.; Tsutsumi, K.; Schärtl, W. Dynamics of Copolymer Micelles in an Entangled Homopolymer Matrix. *Macromolecules* **1999**, *32* (21), 7156–7165.

(22) Hasegawa, R.; Aoki, Y.; Doi, M. Optimum Graft Density for Dispersing Particles in Polymer Melts. *Macromolecules* **1996**, *29* (20), 6656–6662.

(23) Liu, X.; Utomo, N. W.; Zhao, Q.; Zheng, J.; Zhang, D.; Archer, L. A. Effects of Geometric Confinement on Caging and Dynamics of Polymer-Tethered Nanoparticle Suspensions. *Macromolecules* **2021**, *54* (1), 426-439.

(24) Watanabe, H. Rheology of diblock copolymer micellar systems. *Acta polymerica* 48.7 **1997**: 215-233.

(25) Sebastian, J. M., Lai, C., Graessley, W. W., Register, R. A., and Marchand, G. R. (2002). Steady-shear rheology of block copolymer melts: Zero-shear viscosity and shear disordering in body-centered-cubic systems. *Macromolecules* **2002**, *35*(7), 2700-2706.

(26) Sebastian, John M., William W. Graessley, and Richard A. Register. "Steady-shear rheology of block copolymer melts and concentrated solutions: Defect-mediated flow at low stresses in body-centered-cubic systems." *Journal of Rheology* 46.4 **2002**: 863-879.

(27) Daoud, M., and J. P. Cotton. "Star shaped polymers: a model for the conformation and its concentration dependence." *Journal de Physique* 43.3 **1982**: 531-538.

(28) Pham, Q. T., Russel, W. B., Thibeault, J. C., and Lau, W.. Micellar solutions of associative triblock copolymers: Entropic attraction and gas− liquid transition. *Macromolecules*, *32*(9) **1999**, 2996-3005.

(29) Liu, X.; Abel, B. A.; Zhao, Q.; Li, S.; Choudhury, S.; Zheng, J.; Archer, L. A. Microscopic Origins of Caging and Equilibration of Self-Suspended Hairy Nanoparticles. *Macromolecules* **2019**, *52* (21), 8187–8196.

(30) Pakula, T.; Vlassopoulos, D.; Fytas, G.; Roovers, J. Structure and Dynamics of Melts of Multiarm Polymer Stars. *Macromolecules* **1998**, *31* (25), 8931–8940.

(31) Vlassopoulos, D. Macromolecular Topology and Rheology: Beyond the Tube Model. *Rheologica Acta* **2016**, *55* (8), 613–632.

(32) Vlassopoulos, D.; Cloitre, M. Tunable Rheology of Dense Soft Deformable Colloids. *Current Opinion in Colloid & Interface Science* **2014**, *19* (6), 561–574.

(33) Kapnistos, M.; Semenov, A. N.; Vlassopoulos, D.; Roovers, J. Viscoelastic Response of Hyperstar Polymers in the Linear Regime. *The Journal of Chemical Physics* **1999**, *111* (4), 1753–1759.

(34) Gury, L.; Gauthier, M.; Cloitre, M.; Vlassopoulos, D. Colloidal Jamming in Multiarm Star Polymer Melts. *Macromolecules* **2019**, *52* (12), 4617-4623.

(35) Ferreira, P. G.; Ajdari, A.; Leibler, L. Scaling Law for Entropic Effects at Interfaces between Grafted Layers and Polymer Melts. *Macromolecules* **1998**, *31* (12), 3994–4003.

(36) Leibler, L.; Ajdari, A.; Mourran, A.; Coulon, G.; Chatenay, D. Proceedings of the Ordering in Macromolecular Systems, OUMS Conference, Osaka, Japan,(1993). **1994**.

(37) Raphael, E.; Pincus, P.; Fredrickson, G. H. Conformation of Star Polymers in High-Molecular-Weight Solvents. *Macromolecules* **1993**, *26* (8), 1996–2006.

(38) Midya, J.; Rubinstein, M.; Kumar, S. K.; Nikoubashman, A. Structure of Polymer-Grafted Nanoparticle Melts. *ACS nano* **2020**, *14* (11), 15505-15516.

(39) Halim, A.; Fu, Q.; Yong, Q.; Gurr, P. A.; Kentish, S. E.; Qiao, G. G. Soft Polymeric Nanoparticle Additives for next Generation Gas Separation Membranes. *Journal of Materials Chemistry A* **2014**, *2* (14), 4999–5009.

(40) Ahn, S. H.; Park, J. T.; Kim, J. H.; Ko, Y.; Hong, S. U. Nanocomposite Membranes Consisting of Poly (Vinyl Chloride) Graft Copolymer and Surface-Modified Silica Nanoparticles. *Macromolecular research* **2011**, *19* (11), 1195.

(41) Kwon, Y.; Im, H.; Kim, J. Effect of PMMA-Graft-Silica Nanoparticles on the Gas Permeation Properties of Hexafluoroisopropylidene-Based Polyimide Membranes. *Separation and purification technology* **2011**, *78* (3), 281–289.

(42) Ghosal, K.; Freeman, B. D. Gas Separation Using Polymer Membranes: An Overview. *Polymers for advanced technologies* **1994**, *5* (11), 673–697.

(43) Bilchak, C. R.; Jhalaria, M.; Huang, Y.; Abbas, Z.; Midya, J.; Benedetti, F. M.; Parisi, D.; Egger, W.; Dickmann, M.; Minelli, M. Tuning Selectivities in Gas Separation Membranes Based on Polymer-Grafted Nanoparticles. *ACS nano* **2020**. *14* (12), 17174-17183.

(44) Ramesh, N.; Davis, P. K.; Zielinski, J. M.; Danner, R. P.; Duda, J. L. Application of Free-Volume Theory to Self Diffusion of Solvents in Polymers below the Glass Transition Temperature: A Review. *Journal of Polymer Science Part B: Polymer Physics* **2011**, *49* (23), 1629–1644.

(45) Popov, I.; Carroll, B.; Bocharova, V.; Genix, A.-C.; Cheng, S.; Khamzin, A.; Kisliuk, A.; Sokolov, A. P. Strong Reduction in Amplitude of the Interfacial Segmental Dynamics in Polymer Nanocomposites. *Macromolecules* **2020**, *53* (10), 4126–4135.

(46) Ge, S.; Samanta, S.; Tress, M.; Li, B.; Xing, K.; Dieudonné-George, P.; Genix, A.-C.; Cao, P.-F.; Dadmun, M.; Sokolov, A. P. Critical Role of the Interfacial Layer in Associating Polymers with Microphase Separation. *Macromolecules* **2021**, *54* (9), 4246-4256.

(47) Kardasis, P.; Kalafatakis, N.; Gauthier, M.; Vlassopoulos, D.; Floudas, G. Layers of Distinct Mobility in Densely Grafted Dendrimer Arborescent Polymer Hybrids. *Physical Review Letters* **2021**, *126* (20), 207802.

(48) Fetters, L. J.; Lohse, D. J.; Colby, R. H. Chain Dimensions and Entanglement Spacings. In *Physical properties of polymers handbook*; Springer, 2007; pp 447–454.

(49) Guth, E. Theory of Filler Reinforcement. *Journal of applied physics* **1945**, *16* (1), 20–25.

(50) Wolff, S.; Donnet, J.-B. Characterization of Fillers in Vulcanizates According to the Einstein-Guth-Gold Equation. *Rubber chemistry and technology* **1990**, *63* (1), 32–45.

(51) Rubinstein, M.; Colby, R. H. *Polymer Physics*; Oxford University Press New York, 2003.

(52) Snijkers, F.; Ratkanthwar, K.; Vlassopoulos, D.; Hadjichristidis, N. Viscoelasticity, Nonlinear Shear Start-up, and Relaxation of Entangled Star Polymers. *Macromolecules* **2013**, *46* (14), 5702–5713.

(53) Erwin, B. M.; Cloitre, M.; Gauthier, M.; Vlassopoulos, D. Dynamics and Rheology of Colloidal Star Polymers. *Soft Matter* **2010**, *6* (12), 2825.

(54) Parisi, D.; Ruiz-Franco, J.; Ruan, Y.; Liu, C. Y.; Loppinet, B.; Zaccarelli, E.; Vlassopoulos, D. Static and Dynamic Properties of Block Copolymer Based Grafted Nanoparticles across the Non-Ergodicity Transition. *Physics of Fluids* **2020**, *32* (12), 127101.

(55) Pusey, P. N.; Segre, P. N.; Behrend, O. P.; Meeker, S. P.; Poon, W. C. K. Dynamics of Concentrated Colloidal Suspensions. *Physica A: Statistical Mechanics and its Applications* **1997**, *235* (1–2), 1–8.

(56) Zaccarelli, E.; Poon, W. C. Colloidal Glasses and Gels: The Interplay of Bonding and Caging. *Proceedings of the National Academy of Sciences* **2009**, *106* (36), 15203–15208.

(57) Weese, J. A Regularization Method for Nonlinear Ill-Posed Problems. *Computer Physics Communications* **1993**, *77* (3), 429–440.

(58) Elster, C.; Honerkamp, J.; Weese, J. Using Regularization Methods for the Determination of Relaxation and Retardation Spectra of Polymeric Liquids. *Rheologica Acta* **1992**, *31* (2), 161–174.

(59) Honerkamp, J.; Weese, J. A Nonlinear Regularization Method for the Calculation of Relaxation Spectra. *Rheologica acta* **1993**, *32* (1), 65–73.

(60) Ferry, J. D. *Viscoelastic Properties of Polymers*; John Wiley & Sons, 1980.

(61) Bacová, P.; Lentzakis, H.; Read, D. J.; Moreno, A. J.; Vlassopoulos, D.; Das, C. Branch-Point Motion in Architecturally Complex Polymers: Estimation of Hopping Parameters from Computer Simulations and Experiments. *Macromolecules* **2014**, *47* (10), 3362–3377.

(62) Williams, M. L.; Landel, R. F.; Ferry, J. D. The Temperature Dependence of Relaxation Mechanisms in Amorphous Polymers and Other Glass-Forming Liquids. *Journal of the American Chemical society* **1955**, *77* (14), 3701–3707.

(63) Walsh, D.; Zoller, P. *Standard Pressure Volume Temperature Data for Polymers*; CRC Press, 1995.

(64) Kuzuu, N.; Nagai, K.; Tanaka, M.; Tamai, Y. Molecular Dynamics Study of Fictive Temperature Dependence of Density of Vitreous Silica. *Japanese journal of applied physics* **2005**, *44* (10R), 7550.

(65) Milner, S. T.; McLeish, T. C. B. Parameter-Free Theory for Stress Relaxation in Star Polymer Melts. *Macromolecules* **1997**, *30* (7), 2159–2166.

(66) Milner, S. T.; McLeish, T. C. B. Reptation and Contour-Length Fluctuations in Melts of Linear Polymers. *Physical Review Letters* **1998**, *81* (3), 725.

(67) Likhtman, A. E.; McLeish, T. C. Quantitative Theory for Linear Dynamics of Linear Entangled Polymers. *Macromolecules* **2002**, *35* (16), 6332–6343.

(68) Colby, R. H.; Rubinstein, M. Two-Parameter Scaling for Polymers in θ Solvents. *Macromolecules* **1990**, *23* (10), 2753–2757.

(69) Rubinstein, M.; Obukhov, S. P. Power-Law-like Stress Relaxation of Block Copolymers: Disentanglement Regimes. *Macromolecules* **1993**, *26* (7), 1740–1750.

(70) Cai, L.-H.; Panyukov, S.; Rubinstein, M. Hopping Diffusion of Nanoparticles in Polymer Matrices. *Macromolecules* **2015**, *48* (3), 847–862.

(71) Semenov, A. N. Rheology of Polymer Brushes: Rouse Model. *Langmuir* **1995**, *11* (9), 3560–3564.

(72) Witten, T. A.; Leibler, L.; Pincus, P. A. Stress Relaxation in the Lamellar Copolymer Mesophase. *Macromolecules* **1990**, *23* (3), 824–829.

(73) Vlassopoulos, D.; Fytas, G.; Pakula, T.; Roovers, J. Multiarm Star Polymers Dynamics. *Journal of Physics: Condensed Matter* **2001**, *13* (41), R855.

(74) Fetters, L. J.; Kiss, A. D.; Pearson, D. S.; Quack, G. F.; Vitus, F. J. Rheological Behavior of Star-Shaped Polymers. *Macromolecules* **1993**, *26* (4), 647–654.

(75) Johnson, K. J.; Glynos, E.; Sakellariou, G.; Green, P. Dynamics of Star-Shaped Polystyrene Molecules: From Arm Retraction to Cooperativity. *Macromolecules* **2016**, *49* (15), 5669–5676.

(76) Pakula, T., Geyler, S., Edling, T., and Boese, D. Relaxation and viscoelastic properties of complex polymer systems. Rheologica Acta **1996**, 35(6), 631-644.

(77) Sato, T., Watanabe, H., Osaki, K., and Yao, M. L. Relaxation of spherical micellar systems of styrene− isoprene diblock copolymers. 1. Linear viscoelastic and dielectric behavior. *Macromolecules*, *29*(11) **1996**, 3881-3889.

(78) Watanabe, H. Rheology of diblock copolymer micellar systems. *Acta polymerica* 48.7 **1997**: 215-233.

(79) Barbey, R.; Lavanant, L.; Paripovic, D.; Schuwer, N.; Sugnaux, C.; Tugulu, S.; Klok, H.-A. Polymer Brushes via Surface-Initiated Controlled Radical Polymerization: Synthesis, Characterization, Properties, and Applications. *Chemical reviews* **2009**, *109* (11), 5437–5527.

(80) Buenning, E. Ph.D. Thesis. Controllable Free-Volume in Polymer-Grafted Nanoparticle Membranes: Origins, Characterization, and Applications. Columbia University, New York, **2018**.

(81) Gauthier, M.; Munam, A. Synthesis of 1, 4-Polybutadiene Dendrimer- Arborescent Polymer Hybrids. *Macromolecules* **2010**, *43* (8), 3672–3681.

Supporting Information

Universal polymeric-to-colloidal transition in melts of hairy nanoparticles

Daniele Parisi,[1] Eileen Buenning,[2] Nikolaos Kalafatakis,[1] Leo Gury,[1,3] Brian C. Benicewicz,[4] Mario Gauthier[5], Michel Cloitre,[3] Michael Rubinstein,[6,7] Sanat K. Kumar,[2] Dimitris Vlassopoulos[1]

[1] University of Crete, Department of Materials Science and Technology, and FORTH, Institute of Electronic Structure and Laser, Heraklion, Greece.

[2] Department of Chemical Engineering, Columbia University, New York, NY 10025, USA.

[3] Molecular, Macromolecular Chemistry and Materials, ESPCI Paris, CNRS, PSL Research University, 75005 Paris, France

[4] Department of Chemistry and Biochemistry, University of South Carolina, Columbia, SC 29208, USA

[5] Department of Chemistry, Institute for Polymer Research, University of Waterloo, Waterloo, Ontario, Canada N2L 3G1

[6] Departments of Mechanical Engineering and Materials Science, Biomedical Engineering, Chemistry, and Physics, Duke University, Durham, NC 27708, USA

[7]Institute for Chemical Reaction Design and Discovery (WPI-ICReDD), Hokkaido University, Sapporo 001-0021, Japan

Table of Contents

1. Conceptualization of colloidal jamming

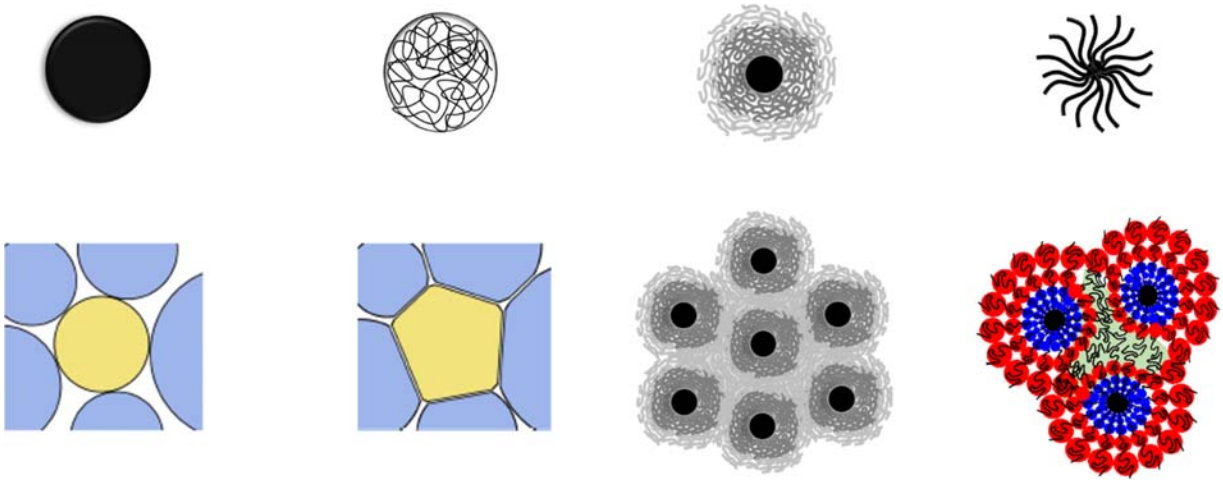

Figure S1. Illustrative sketches of different nanoparticles (top) and their jammed state (bottom). From left to right: hard spheres with one-dimensional contacts, soft impenetrable microgels (no dangling ends) with two-dimensional faceting, jammed GNPs and stars with three-dimensional interpenetration (green-shaded interstitial region).

2. Linear viscoelastic measurements and analysis

As the silica content increases (more than 5% in volume of silica), a small horizontal shift of the linear viscoelastic master curves was detected at the same reference temperature, namely for the 94k, 48k, and 33k samples (see Table 1). The horizontal shift increases with the content of silica towards lower frequencies, as expected for systems exhibiting higher glass transition temperature T_g. By horizontally translating the master curves of the above-mentioned three systems to make the Kuhn monomer relaxation time (τ_0) values coincide, it is possible to estimate the increase in the average glass transition temperature due to the presence of silica: $\Delta T = T - T_{ref}(60°C)$. By applying the William-Landell-Ferry (WLF) equation,[2] $\log a_T = -\frac{C_1(T-T_{ref})}{C_2+((T-T_{ref})}$ with C_1 and C_2 being the WLF coefficients and T_{ref} the reference temperature, it is possible to calculate the

deviation from the reference temperature, therefore the increase in T_g, which amounts to 1.5 °C, 2.5 °C, and 3.7 °C for the samples 94k, 48k and 33k, respectively. The dynamic response appears very sensitive to small differences in T_g among the samples with different silica volume fractions. The apparent disagreement with differential scanning calorimety (DSC) measurements for determining the T_g, and reported in the main text, is well known and reported in several publications.[3–6] We have not looked in detail at the segmental dynamics and have not examined the validity of the time-temperature superposition near T_g. There is evidence for a T_g gradient and associated different layers of local mobility in the vicinity of the nanoparticles.[7,8] However, as the present work focuses on long-time dynamics, the differences in local dynamics have not been investigated in more detail. In general, changes in mechanical properties through a transition are proportionally larger than changes in specific heat. In these dynamic mechanical analysis (DMA) measurements, besides the differences in the temperature profiles, which already play an important role in the glass transition, another variable needs to be taken into account: the measurement time. This is the reason why the glass transition temperature obtained through dynamic measurements is usually called dynamic T_g.[9–11] An investigation by Garcia-Fernandez[6] confirmed that, if different dynamic techniques (DMA and temperature-modulated DSC) with the same frequency response and temperature profile are used to determine T_g, the obtained values are exactly the same. All the shifted master curves are shown in Figure S2 for the same temperature offset from the dynamic T_g.

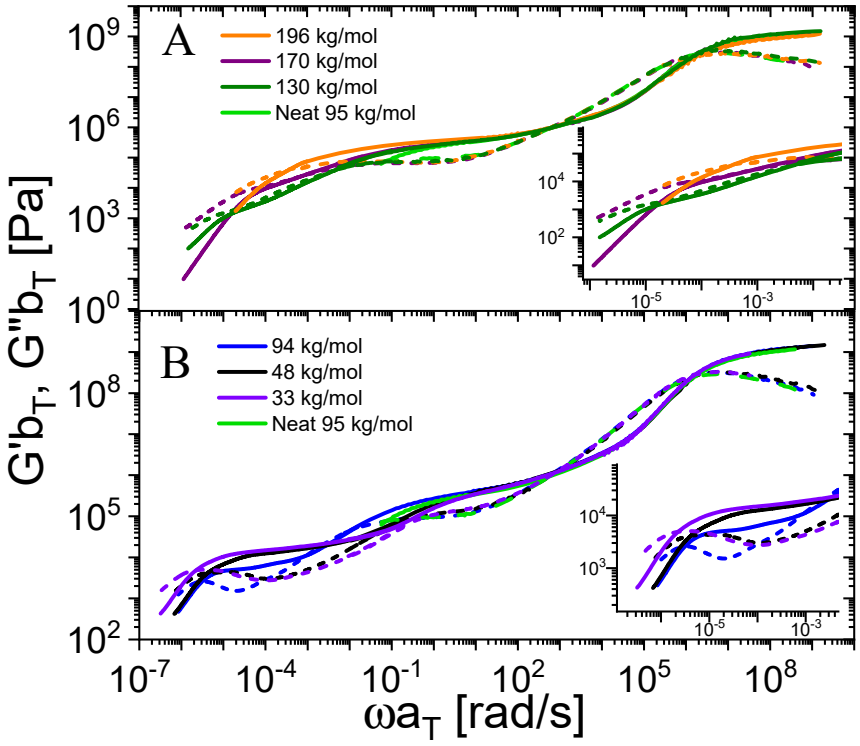

Figure S2. Linear viscoelastic master curves in terms of shifted $G'b_T$ (solid lines) and $G''b_T$ (dashed lines) as functions of shifted oscillatory frequency ωa_T. The curves were shifted at the same distance from the glass transition temperature. The four lowest frequency decades were obtained by creep data conversion into dynamic moduli. The data are presented in two panels, A and B, for clarity of presentation. The insets in both panels are magnifications of the low-frequency region.

To validate the accuracy of the time-Temperature Superposition (tTS) principle, a frequency-independent plot can be used, the so-called van Gurp-Palmen plot (vGP),[12] where the phase angle is plotted against the complex modulus (see Figure S3). This representation is very sensitive in detecting rheological complexities. The vGP plot has been shown to be a particularly useful indicator of thermorheological complexities in a variety of branched and polydisperse macromolecular systems.[13–16] The applicability of the TTS reflects a homogeneous distribution of monomeric friction in the system, as in the case of linear polymer melts, for which the monomeric time is a kind of internal clock in the system and any relaxation time is in effect a superposition of different times, all dependent on monomeric friction.[17] Hence, the temperature dependence of the relaxation time is directly proportional to the temperature dependence of the monomeric friction coefficient.

The vGP plots for the systems investigated are provided in Figure S3. The first four lowest decades in complex modulus were obtained through creep conversion so that those data were not subjected to time-temperature superposition, as the creep experiments were performed at T-T_g = 40 °C. Above about 10^5 Pa, TTS was applied and no signature of thermorheological complexities can be observed, implying that despite the colloidal nature of the system, particle-particle friction is still controlled by the polymer chains and it is homogeneously distributed over the system.[8]

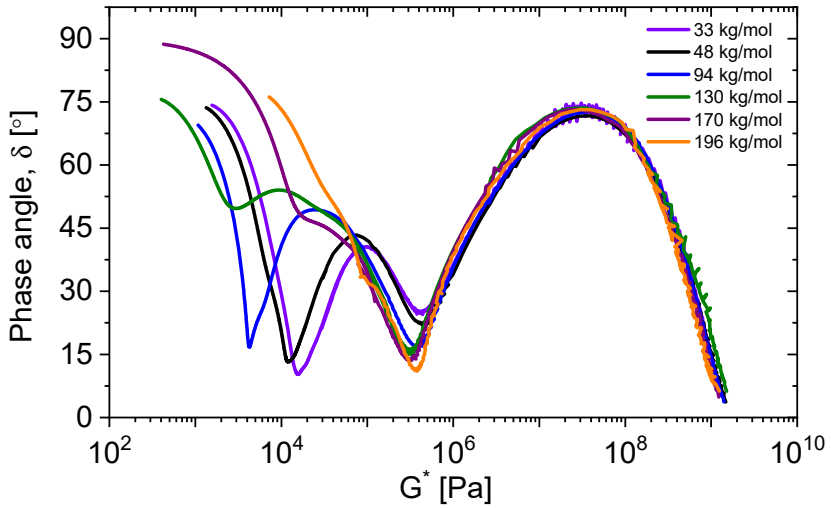

Figure S3. Phase angle as a function of the complex modulus (van Gurp-Palmen representation). The curves were shifted to the same distance from T_g.

The following table reports the experimental characteristic times and plateau moduli at T-T_g = 40, °C estimated from Figure 1B of the main text. From high to low frequencies we can detect in sequence: the relaxation time of a Kuhn monomer τ_0, the Rouse relaxation time of an entanglement strand τ_e, the arm retraction time τ_{arm} and the structural or terminal relaxation time τ_{term}. Note that τ_0 and τ_{arm} refer to the inverse frequency at the relative maxima in tan(δ), which imply a maximum viscous dissipation in the system, while τ_e and τ_{term} are estimated as the inverse frequency at which tan(δ) = 1.[17,18] The relaxation time of a Kuhn monomer τ_0, and of an entanglement strand τ_e are

independent of the chain degree of polymerization, and take values of 1.98×10^{-5} s and 0.002 s, respectively, at $T = T_g$+40 °C.

Table S1. Characteristic relaxation time at T-T_g = 40 °C and plateau moduli.

M_w [kg/mol]	τ_{arm} [s]	τ_{term} [s]	G_{LF} [kPa]	$G_{plateau}$ [kPa]
196	2439.0	2439.0	-	262
170	222.2	16949.1	-	265
130	80.0	43333.0	2	270
94	41.7	406504.1	4	276
18	12.7	194117.6	13	317
33	2.5	357143.0	14	350

The creep compliance data at 60 °C and 3 different stresses (50, 80 and 100 Pa) are provided in Figure S4 for the 94k sample. Different stresses resulted in the same temporal evolution of the deformation. This confirms that the material was probed in the linear viscoelastic regime. The retardation spectrum obtained with the NLREG[19,20] software also shows a good agreement between different stresses (see Figure S5). The data exhibit a lower minimum around 5000 s, slightly more pronounced at 50 Pa, which coincides with the shoulder observed in the compliance. Nevertheless, it is important to note that the method is independent on the range of data taken into account for the conversion as measurements at different stresses terminate at different times. Dynamic compliances and converted moduli are shown in Figures S6 and S7, respectively. Note that for the conversion to dynamic moduli the first two highest frequency decades (0.01 – 1 s in the time domain) were discarded as creep compliance data at short times are noisy.

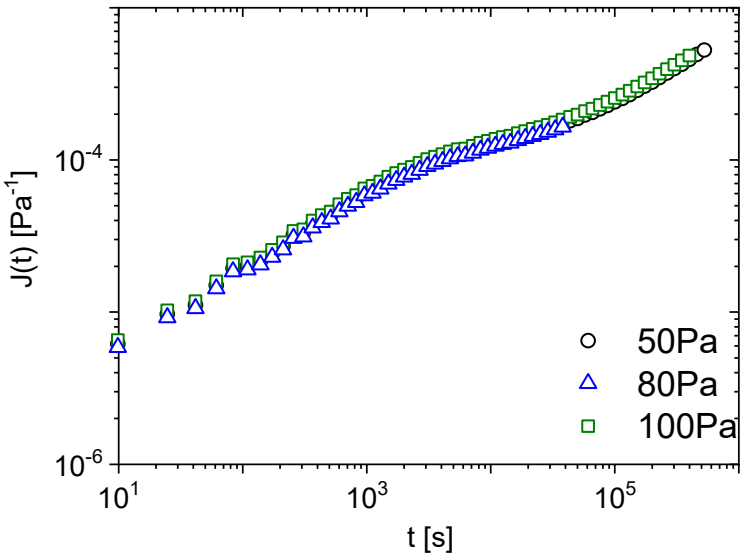

Figure S4. Creep compliance versus time for the GNP 94k at 60 °C. Three different stresses were used in order to confirm that the measurements took place in the linear viscoelastic regime.

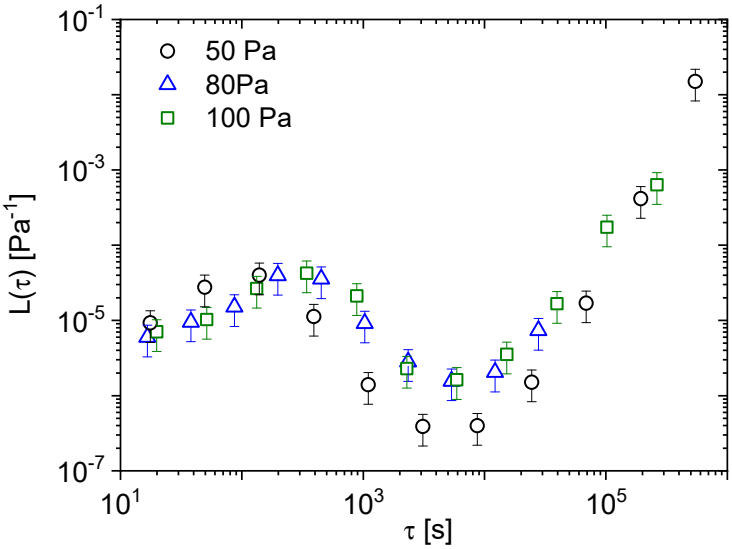

Figure S5. Retardation spectrum for the GNP 94k at 60 °C. Three different stresses were used in order to confirm that the measurements took place in the linear viscoelastic regime. Note that the maximum in the retardation spectrum occurs on a time scale (about 300s) that exceeds the inverse of the typical frequency range probed in the dynamic frequency sweep (DFS) experiments (0.01 rad/s).

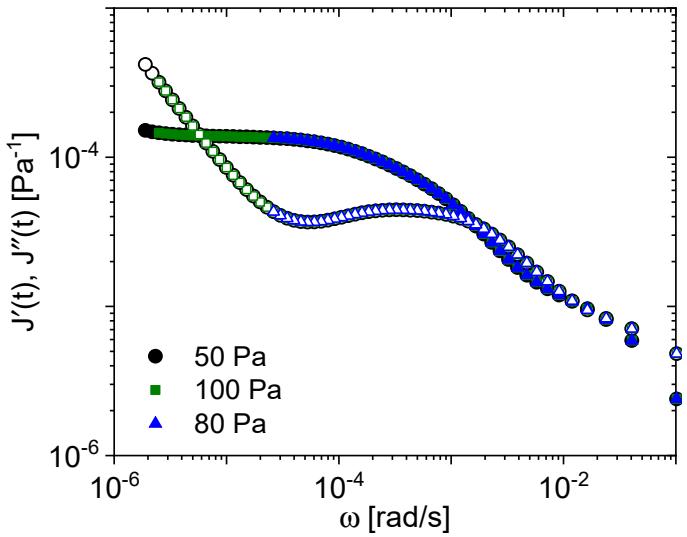

Figure S6. Converted dynamic compliances of the GNP 94k at 60 °C and 3 different stresses: 50, 80 and 100 Pa.

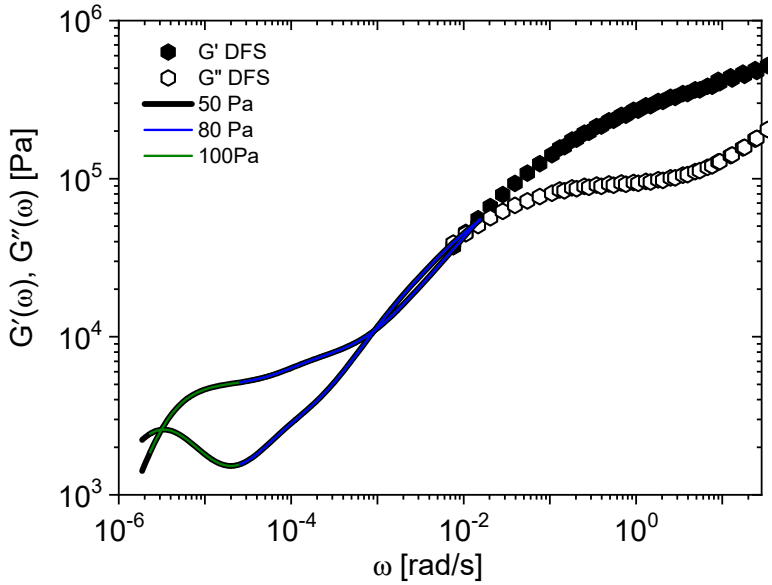

Figure S7. Converted dynamic moduli from creep experiments as a function of oscillatory frequency (lines) along with dynamic frequency sweep (DFS) data (hexagons) for the GNP 94k at 60 °C and 3 different stresses: 50, 80 and 100 Pa. The data at $\omega > 30$ rad/s are not shown to emphasize the converted creep compliance data.

The dependence of the plateau modulus normalized by the modulus of the neat PMA polymer as a function of the silica volume fraction, is displayed in Figure S8. The increase in the plateau

modulus, resulting from filler reinforcement effects, follows the Guth-Gold[21,22] phenomenological expression

$$\frac{G(\Phi)}{G(\Phi=0)} = 1 + 0.67\beta\Phi + 1.62(\beta\Phi)^2 \qquad (S1)$$

with β being an effective shape factor (proportional to length/width of the filler) which in this case takes the value 4.3 (even though the silica particles were spherical) to fit the strong reinforcement observed experimentally, and Φ is the silica volume fraction estimated from thermal gravimetric analysis (TGA) experiments[23] and reported in Table M1 in the main text.

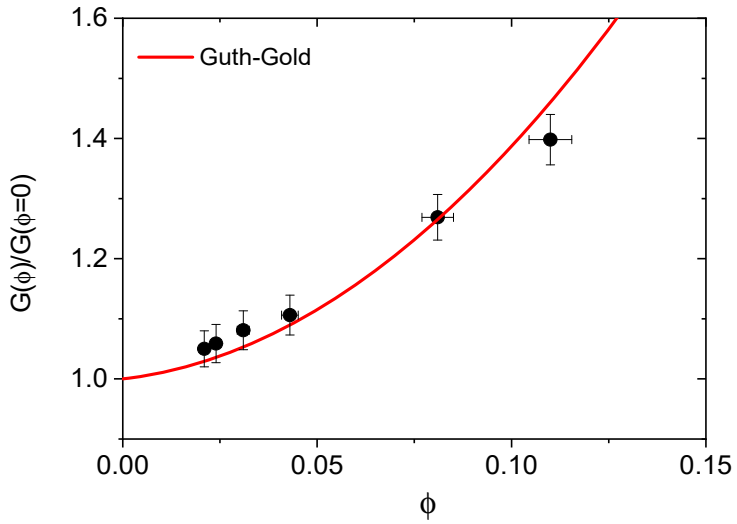

Figure S8. Plateau modulus of GNPs normalized by that of a PMA neat polymer (95 kg/mol) as a function of silica volume fraction. The solid red line represents eq. S1. The plateau modulus refers to the storage modulus corresponding to the minimum in the loss factor *tan(δ)* (see Figure 1B in the main text). The errors in the determination of the minimum in *tan(δ)* and polydispersity of the silica core are also reported as vertical and horizontal error bars, respectively.

Linear viscoelastic curves are displayed in Figures S9 and S10 in terms of complex viscosity η*(ω), and stress relaxation modulus (G(t)) respectively. Both representations were used to estimate the zero-shear viscosity (η_0) depicted in Figure S12 below. The complex viscosity was fitted to the Cross-like function[24] (solid lines in Fig. S9B) to determine the extrapolated zero-shear viscosity, and the fitting parameters used are listed in Table S2.

$$\eta^*(\omega) = \eta_0/(1 + (\tau\omega)^m) \qquad (S2)$$

Table S2. Fitting parameters obtained from the Cross model.

M_w [kg/mol]	η_0 [Pa·s]	τ [s]	m
196	$4.5\ 10^8$	$6.7\ 10^3$	0.74
170	$3.9\ 10^8$	$1.4\ 10^4$	0.95
130	$3.6\ 10^8$	$1.2\ 10^5$	0.7
94	$2.2\ 10^9$	$3.2\ 10^5$	0.96
48	$2.7\ 10^9$	$2.3\ 10^5$	0.94
33	$5.4\ 10^9$	$3.5\ 10^5$	0.95

Alternatively, the zero-shear viscosity (η_0) can be calculated as the integral $\int_0^t G(t)td(lnt)$. The molar mass dependence of the zero-shear viscosity is shown in Figure S11 for the GNPs, as well as for the linear chains (η_{lin}) used for normalization in Figure S12. The viscosity values are reported in Table S3. The latter also includes the viscosity estimated directly from creep experiments.

Table S3. Viscosity values at 60 °C.

M_w [kg/mol]	η_{term} *(integral)* [Pa·s]	η_{term} *(creep)* [Pa·s]	η_{lin} [Pa·s]
196	$5.18\ 10^8$	$4.92\ 10^8$	$2.32\ 10^6$
170	$3.48\ 10^8$	$3.81\ 10^8$	$8.98\ 10^5$
130	$3.33\ 10^8$	$3.54\ 10^8$	$4.23\ 10^5$
94	$1.75\ 10^9$	$2.25\ 10^9$	$2.36\ 10^5$
48	$2.60\ 10^9$	$2.72\ 10^9$	$2.92\ 10^4$
33	$6.00\ 10^9$	$5.88\ 10^9$	$1.07\ 10^4$

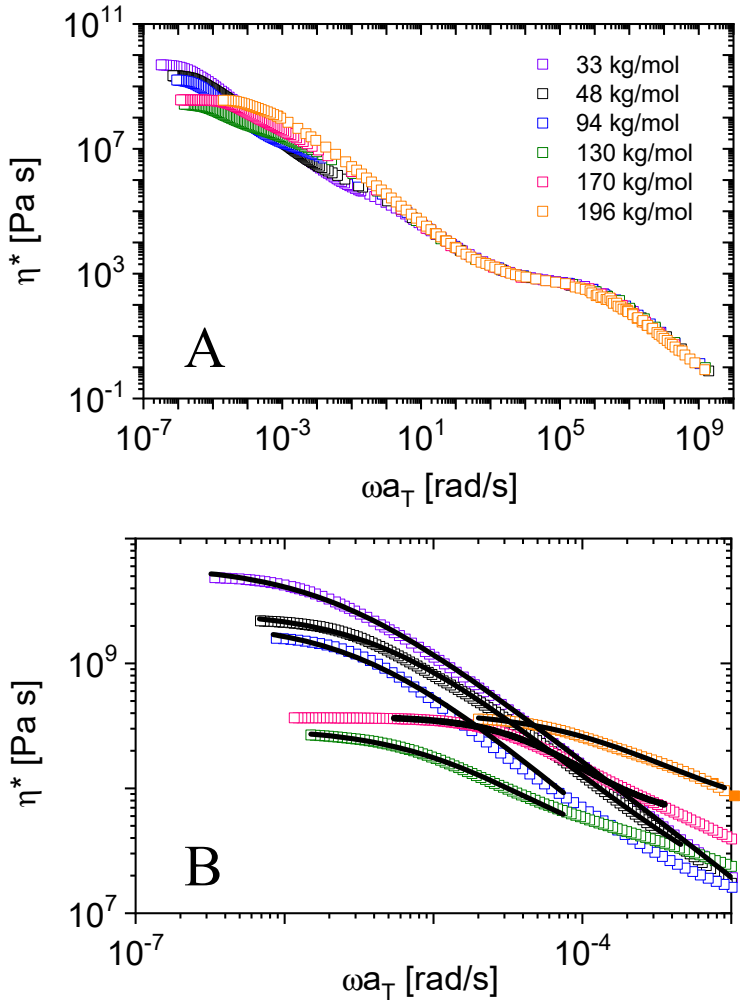

Figure S9. A) Linear viscoelastic master curves from Figure S2 in terms of complex viscosity as a function of shifted angular frequency. B) Magnification of the low-frequency region reported in Panel A. The black solid lines represent fits to the Cross model (eq. S2) to determine the zero-shear viscosity. Note that only the creep compliance data converted into dynamic moduli were used for the fits.

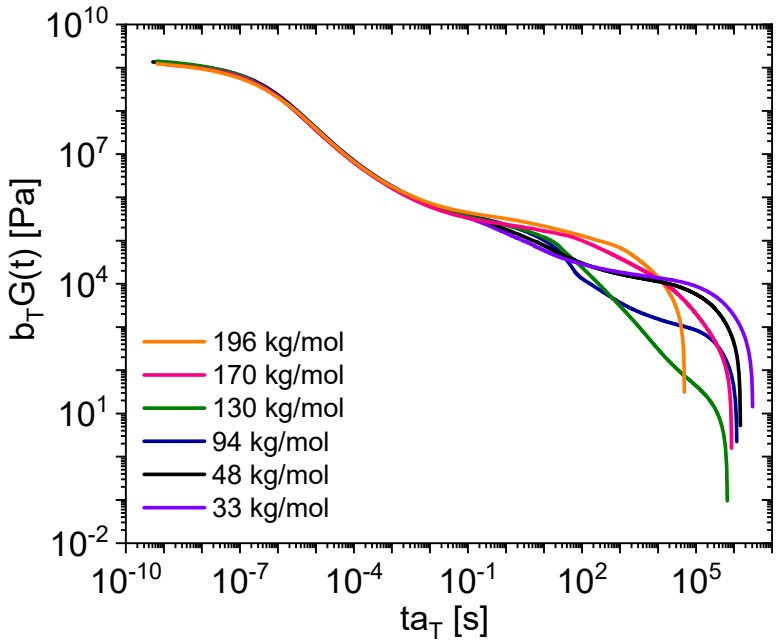

Figure S10. Linear viscoelastic master curves from Figure S2 converted into stress relaxation modulus as a function of time.[2]

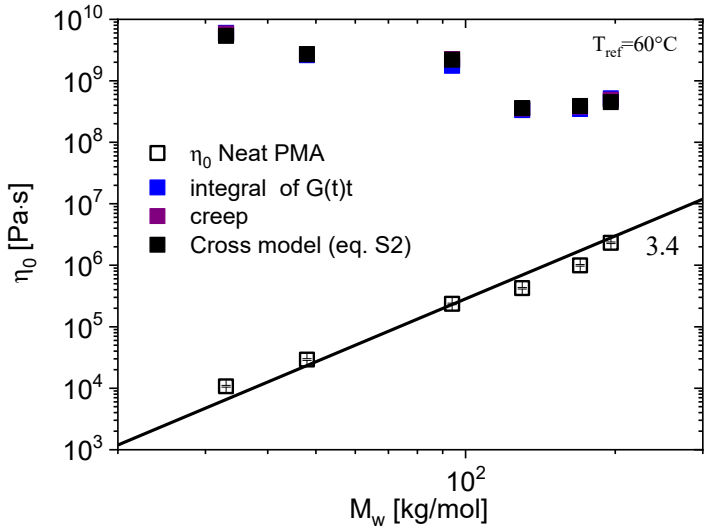

Figure S11. Arm molar mass dependence of the zero-shear viscosity for the GNPs estimated from eq. S2 (black squares), the integral of G(t)t (see text) (blue squares), and creep experiments (see Tables S2 and S3). The zero-shear viscosity of neat linear PMA melts is reported as open squares. The black solid line represents the expected 3.4 slope for entangled linear polymer chains.[17] All the viscosity values are reported at 60 °C.

3. A simple brush conformation model[1]

Several approaches to describe the brush regime of densely grafted spherical particles either in a solvent or in the presence of a matrix of linear polymer chains have been discussed in the literature.[25–33] In the present case, the nanoparticles were in a solvent-free state; therefore incompressibility and space-filling conditions represented key elements for a simple model, namely the two-layer model, developed by Midya *et al.*[1] to examine the transition from dry to interpenetrated brush regimes. The former represents the portion of the generic grafted chain close to the core and is relatively stretched because of steric hindrance due to the presence of neighboring chains grafted to the core (one may think of this section as containing virtually no monomers from the chains grafted onto other NPs, hence "dry"), whereas the latter constitutes the "active" chain sections that overlap and form entanglements with chains grafted onto neighboring particles. This constitutes the interpenetration layer. The concept behind this model is represented in Figure S12, where the generic grafted chain contains N_{arm} Kuhn monomers divided into g monomers located in the dry layer (h_{dry}) and $N_{inter} = N_{arm}$-g in the interpenetration layer ($h_{inter}/2$). The radius $R_{core+dry}$, which includes the core and the dry layer, determines the boundary between dry and interpenetrated regions. The total radius of the particle can be written as:

$$R = \left[\left(R_{core}^3 + \frac{3}{4\pi} v_0 f N_{arm}\right)\right]^{\frac{1}{3}} \qquad (S3)$$

with $v_0 = \frac{M_0}{N_A \rho}$ being the volume of a Kuhn monomer (v_0 =0.673 nm^3 with M_0= 494.6 g/mol[34] and ρ = 1.22 g/cm^3 [35]), f the functionality and R_{core} the radius of the core.

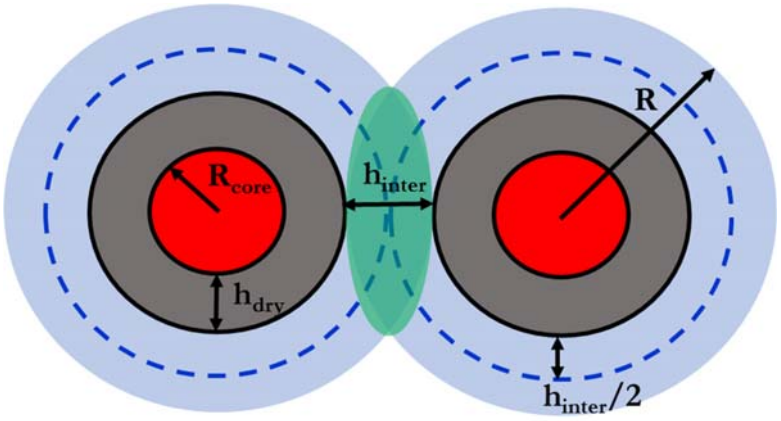

Figure S12. Schematic representation of two interpenetrated grafted nanoparticles with a set grafting density. R_{core} is the radius of the core, while h_{dry} and $h_{inter}/2$ are the thicknesses of the dry and interpenetrated layers, respectively. The layer of thickness h_{dry} contains g Kuhn monomers, whereas the interpenetration zone comprised N_{arm}-g monomers, with N_{arm} being the total Kuhn degree of polymerization of the graft. The radius R represents the total size of the grafted nanoparticles, estimated from eq. S3.

The governing equations of the simplified model proposed by Midya *et al.*[1] follow. The monomer space-filling condition leads to:

$$\frac{4\pi}{3}\left[\left(R_{core}+h_{dry}\right)^3-R_{core}^3\right]=fgv_0 \tag{S4}$$

An analogous expression can be formulated for the interpenetration layer:

$$\frac{4\pi}{3}\left[\left(R_{core}+h_{dry}+h_{inter}/2\right)^3-\left(R_{core}+h_{dry}\right)^3\right]=fN_{inter}v_0 \tag{S5}$$

Under the assumption that in the interpenetration zone outside the dry layer, polymer chains exhibit a Gaussian conformation, the thickness of the interpenetration layer reads as

$$h_{inter}=0.93b(N_{arm}-g)^{1/2} \tag{S6}$$

with b being the Kuhn length (b = 1.47 nm) and 0.93 a prefactor used by Midya *et al.*[1] to match simulations and theoretical predictions.

The total thickness of the brush can be written as:

$$h=h_{dry}+\frac{h_{inter}}{2}=R-R_{core} \tag{S7}$$

Equations S1-S5 can be rearranged to obtain an analytical solution for the number of monomers in the dry zone (g) (note that the number of monomers in the interpenetration zone can be trivially obtained from the difference $N_{arm} - g$):

$$g = N_{arm} - \left(\frac{3fv_0}{\pi b^3}\right)^2 \left(\frac{1}{x} + 1\right)^2 \left(1 - \sqrt{1 - \frac{4}{3}\left(\frac{1}{1+x}\right)^2}\right)^2 \quad \text{(S8)}$$

where x is the "overcrowding" parameter defined as:

$$x = \frac{f}{\frac{\pi b^2}{v_0}\left(R_{core}^3 + \frac{3fN_{arm}v_0}{4\pi}\right)^{1/3}} \quad \text{(S9)}$$

The overcrowding parameter is the ratio between the number of grafted chains in the GNPs and the maximum number of unperturbed chains with the same molar mass that can be present in the same volume occupied by the polymeric corona. If this parameter is equal to one, the system corresponds to an unperturbed melt. On the contrary, for $x > 1$, the volume is overcrowded and the grafted chains are significantly stretched. For $x < 1$ the grafted chains (or star arms) significantly interpenetrate.

An alternative way to calculate h_{inter} is that using the star polymer brush conformation model, initially developed by Kapnistos *et al.,*[36] and recently modified by Midya *et al.*[1] to account for the presence of a rigid core. In this case, the thickness of the interpenetration is written as[1]

$$h_{inter} = 0.9b(N_{arm} - g)^{1/2}x^{-1/6} \quad \text{(S10)}$$

where 0.9 is a prefactor needed to match the simulations results.[1] As shown in the main text, as well as in Ref. 1, the two models yield similar results (albeit not identical, since the Kapnistos *et al.,*[36] model considers that the number of arms in the interpenetration zone is smaller than *f*).

The quantities obtained from the brush conformation model, the fit to the Milner-McLeish model, as well as the modified Kapnistos *et al.*[36] predictions for star-polymers are reported in Table S5. The volume fraction of the core plus the dry layer can be written as follows and is also reported in Table S4 below:

$$\phi_{core+dry} = \frac{\frac{4\pi}{3}R_{core}^3 + v_0 f g}{v_0 f N_{arm} + \frac{4\pi}{3}R_{core}^3} \qquad (S11)$$

The Kuhn degree of polymerization of the interpenetration zone estimated from the MM model, N_{seff}, is reported in Figure S13A (open and filled circles) as a function of the total Kuhn degree of polymerization of the grafted arms. Note however that this is a model for dynamics rather than structure and, moreover, that for the two lowest N_{arm} values with Z < 5 (filled circles) the applicability of the MM model is questionable. Indeed, for these systems, fitting analysis using the MM model suggests that the entire arm participates in the retraction process. Therefore, a more rigorous determination of the interpenetrated layer, N_{inter}, is needed. This is possible using the two-layer brush conformation model, for which results are shown in Figure S13A. Once the average degree of polymerization of an arm in each layer is known, the respective thicknesses can be estimated from eq. S10 (Figure 13B). To examine the sensitivity of the two-layer brush conformation model to polydispersity, we performed and report in Figure S14 a parametric study in terms of fraction of the dry layer for the investigated GNPs with varying core size and grafting density (see eqs. S3, S6 and S7). Polydispersity was not taken into account in the analysis of the colloidal cage escape mode. Note that nearly identical results can be obtained with the colloidal star model of Kapnistos *et al.*[36], as modified by Midya *et al.*[1] to account for the presence of a core (results not shown).

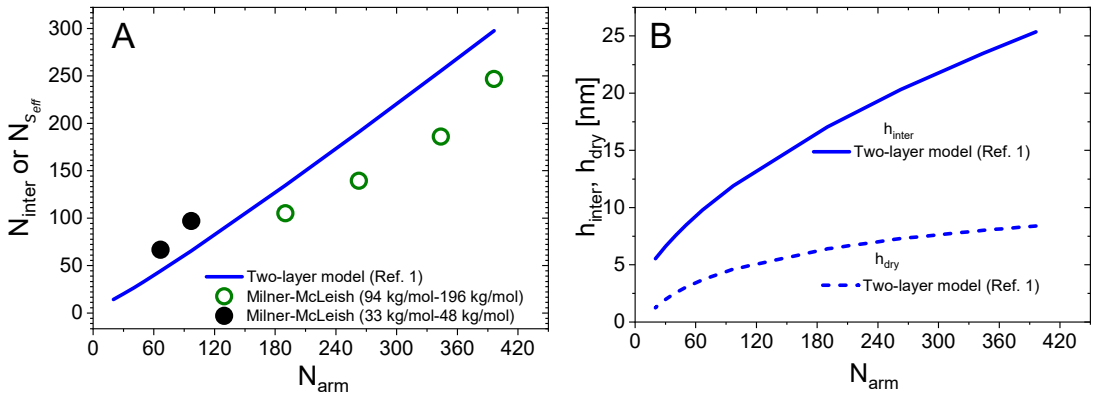

Figure S13. (A) Kuhn degree of polymerization of the interpenetration layer obtained from (i) the fits of the linear viscoelastic master curves (polymeric response) with the MM model (open and filled circles), $N_{s_{eff}}$, (ii) the two-layer model[1] (blue line), N_{inter}, as a function of the total Kuhn degree of polymerization N_{arm}. Based on the linear viscoelastic spectra, the viscoelastic liquid-to-jammed transiton seems to occur at about N_{arm} = 190. (B) Predicted thickness of the interpenetration (solid lines) and dry (dashed line) layers as a function of N_{arm}.

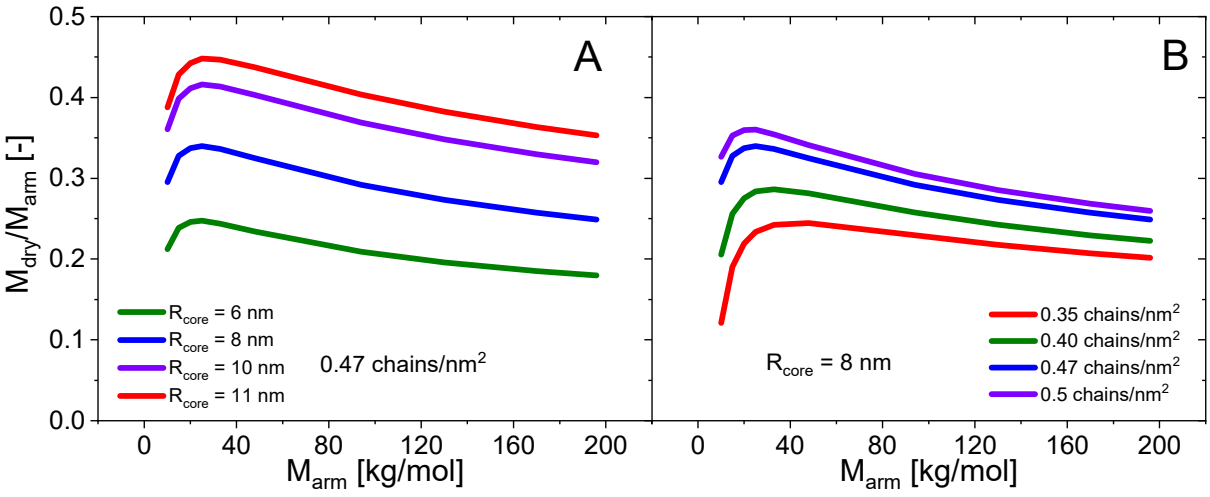

Figure S14. Effects of core size (Panel A) and grafting density (Panel B) on the molar mass of the dry layer over the total arm molar mass, as a function of the total arm molar mass. The two-layer model was used for this parametric study.

4. Modeling of polymeric arm relaxation

The experimental linear viscoelastic spectra are shown in Figures S15-S20, together with the Milner-McLeish (MM) model[36,37] (see main text for details) applied in two different ways: i) best fit to the experimental data with s_{eff} as a fitting parameter (blue lines) and ii) using N_{inter}, therefore s_{eff}, estimated from the two-layer model (red lines).

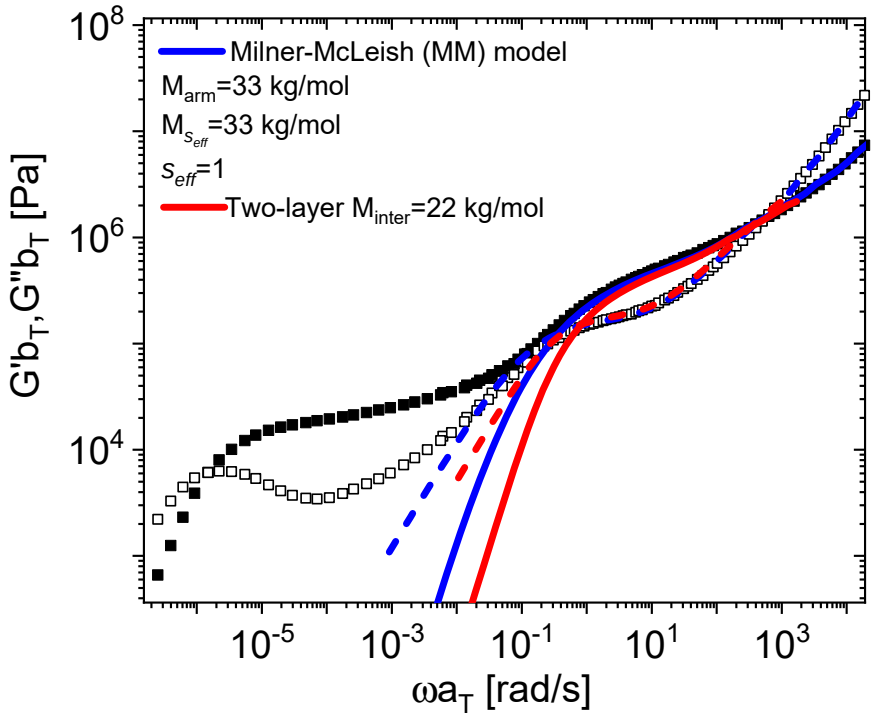

Figure S15. Linear viscoelastic master curves in terms of shifted $G'b_T$ (solid symbols) and $G''b_T$ (open symbols) as functions of the shifted oscillatory frequency ωa_T *at* $T\text{-}T_g = 40°C$ for the GNP 33k sample. The solid blue lines represent MM model fitting curves with adjustable parameter s_{eff}. M_{arm} is the arm molar mass, s_{eff} is the average fraction of arm in the interpenetrated layer, corresponding to a molar mass M_{seff}. As discussed in the text, in reality the arm length of the interpenetrating arms fluctuates,[36,38] but this is not taken into account in our analysis. This is also the case for the other related figures (S16-S20).

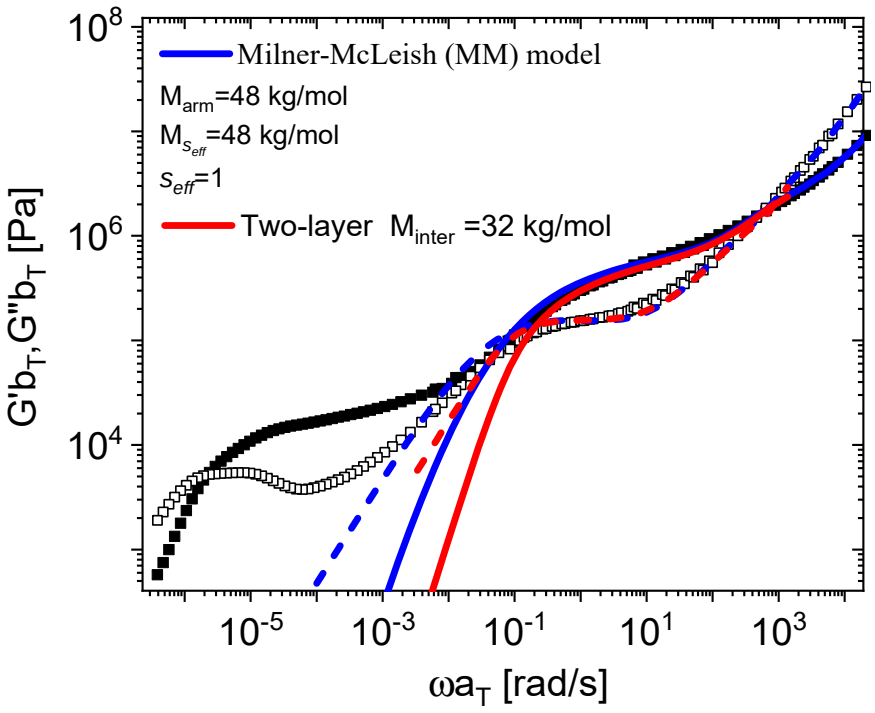

Figure S16. Linear viscoelastic master curves in terms of shifted G′b_T (solid symbols) and G″b_T (open symbols) as functions of the shifted oscillatory frequency ωa_T at T-T_g = 40°C for the GNP 48k sample. The solid blue lines represent MM model fitting curves with adjustable parameter s_{eff}. M_{arm} is the arm molar mass, s_{eff} is the average fraction of arm in the interpenetrating layer, corresponding to a molar mass $M_{s_{eff}}$. Note that especially for the two shortest GNPs, in one part of the layer the overlap is stronger than in another part. This, along with other reasons (such as the approximate nature of eq.1 of the main text) may explain the larger M_{seff} (which is actually equal to M_{arm}) as compared to M_{inter}.

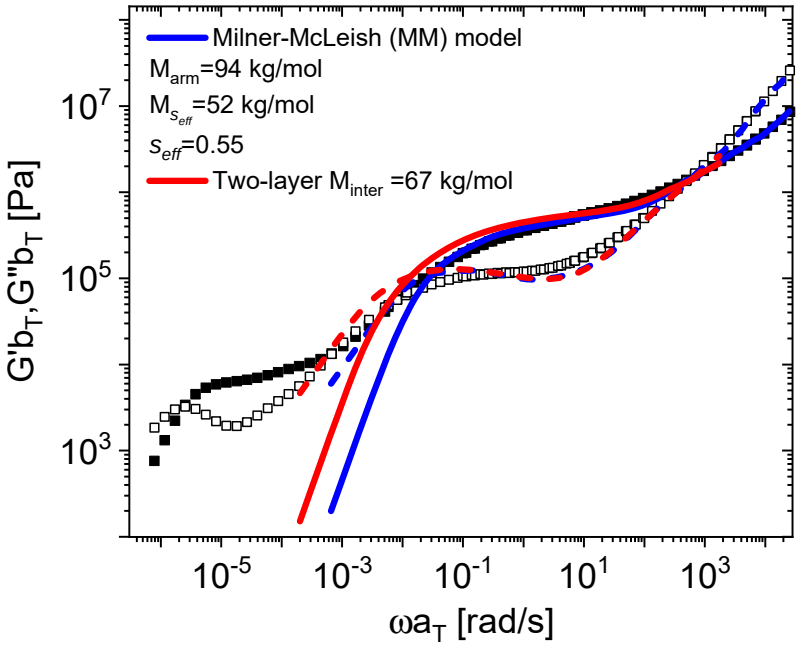

Figure S17. Linear viscoelastic master curves in terms of shifted $G'b_T$ (solid symbols) and $G''b_T$ (open symbols) as functions of the shifted oscillatory frequency ωa_T at $T\text{-}T_g = 40°C$ for the GNP 94k sample. The solid blue lines represent MM model fitting curves with adjustable parameter s_{eff}. M_{arm} is the arm molar mass, and s_{eff} is the fraction of the arm in the interpenetrating layer, corresponding to a molar mass $M_{s_{eff}}$.

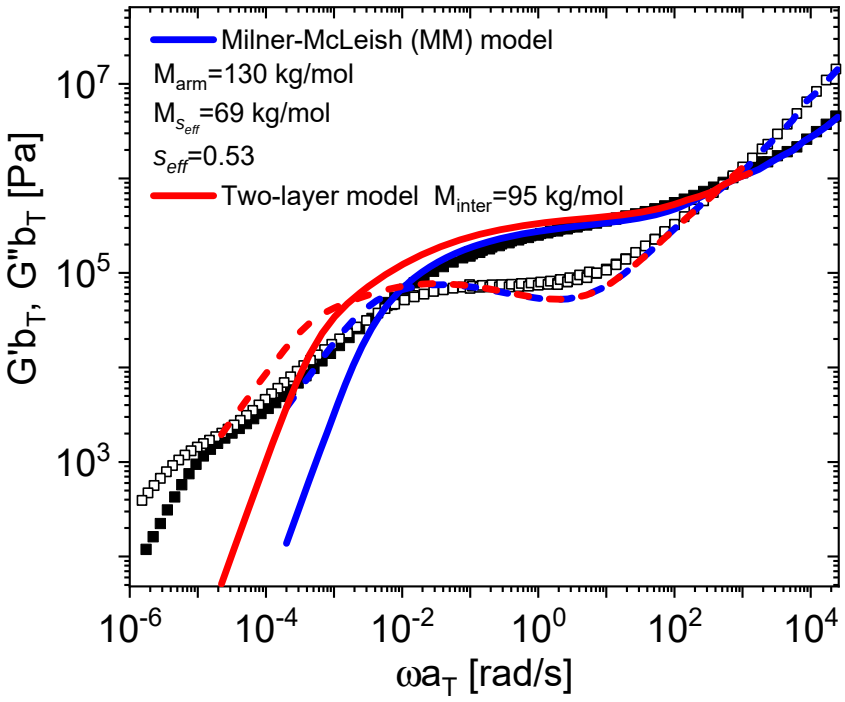

Figure S18. Linear viscoelastic master curves in terms of shifted $G'b_T$ (solid symbols) and $G''b_T$ (open symbols) as functions of the shifted oscillatory frequency ωa_T at $T\text{-}T_g = 40°C$ for the GNP 130k sample. The solid blue lines represent MM model fitting curves with adjustable parameter s_{eff}. M_{arm} is the arm molar mass, and s_{eff} is the fraction of arm in the interpenetrating layer, corresponding to a molar mass M_{seff}.

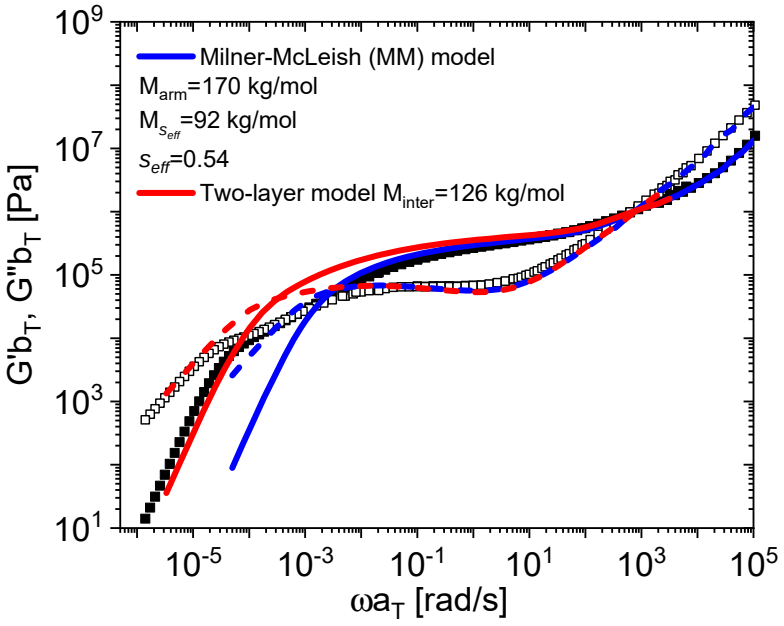

Figure S19. Linear viscoelastic master curves in terms of shifted $G'b_T$ (solid symbols) and $G''b_T$ (open symbols) as functions of the shifted oscillatory frequency ωa_T at $T\text{-}T_g = 40°C$for the GNP 170k sample. The solid blue lines represent MM model fitting curves with adjustable parameter s_{eff}. M_{arm} is the arm molar mass, s_{eff} is the fraction of the arm in the interpenetrated layer, corresponding to a molar mass M_{seff}.

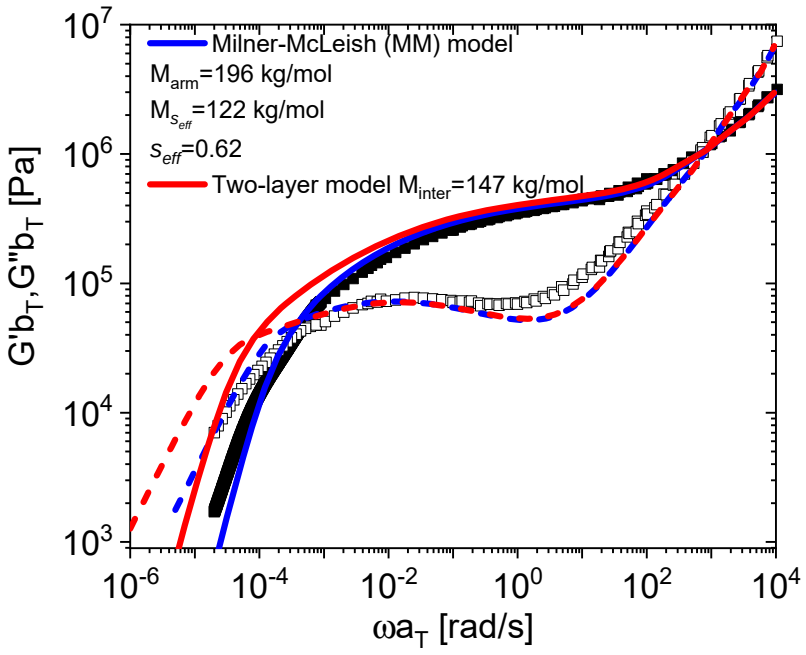

Figure S20. Linear viscoelastic master curves in terms of shifted $G'b_T$ (solid symbols) and $G''b_T$ (open symbols) as functions of the shifted oscillatory frequency ωa_T at $T\text{-}T_g = 40°C$ for the GNP 196k sample. The solid blue lines represent MM model fitting curves with adjustable parameter s_{eff}. M_{arm} is the arm molar mass, and s_{eff} is the fraction of arm in the interpenetrating layer, corresponding to a molar mass M_{seff}.

The main results obtained by fitting the rheological data with the Milner-McLeish model are summarized in Table S4. M_{seff} and M_{inter} are the molar mass of the interpenetrated region, according to the best fit to the experimental data of the MM model and the predictions of the two-layer model, respectively. Similarly, $\tau_{arm,seff}$ and τ_{arm} are the relaxation time of the polymeric response from the best fit and the two-layer model, respectively (see also Figures S15-S20).

Table S4. Molecular characteristics, and characteristic relaxation time based on analysis with the Milner-McLeish model.

M_{arm} [kg/mol]	N_{arm} [-]	M_{seff} [kg/mol]	$\tau_{arm,seff}$ [s]	M_{inter} [kg/mol]	τ_{arm} [s]
196	396	122	2463	147	11905
170	344	92	390.6	126	3141
130	263	69	129.9	94	649
94	189	52	30.3	67	77
48	97	48	7.1	32	4.4
33	67	33	1.8	22	1.2

Table S5. Comparison between different models accounting for the interpenetrated layer of GNPs

Analysis based on two-layer model[1]						
M_{arm} [kg/mol]	N_{arm} [-]	g [-]	M_{dry} [kg/mol]	N_{inter}	M_{inter} [kg/mol]	$\phi_{core+dry}$ [-]
196	396	98.7	49	298	147	0.26
170	344	88.5	44	255	126	0.28
130	263	71.9	35	191	94	0.30
94	190	55.5	27	134	67	0.32
48	97	31.5	16	65	32	0.38
33	67	22.4	11	44	22	0.41
Analysis based on Kapnistos *et al.* model[36]						
196	396	99	49	298	147	0.26
170	344	89	44	254	126	0.28
130	263	74	37	189	93	0.30
94	190	58	29	132	65	0.34
48	97	34	17	63	31	0.40
33	67	25	12	42	21	0.45
Analysis based on Milner-McLeish model for arm relaxation (this work)						
196	396	150	74	247	122	0.39
170	344	158	78	186	92	0.47
130	263	123.	61	139	69	0.48
94	190	85	42	105	52	0.47
48	97	0	0	97	48	0.08
33	67	0	0	66	33	0.11

5. Slow (colloidal) mode analysis

The generic GNP shown in Figure 4 of the main text has an initial (before deformation) overall radius R (eq. S3) while the initial grafted arm size is $h_{pol} = R - R_{core}$, and the respective deformed sizes are D and $h'_{pol} = [R^2 - D^2 + (D - R_{core})^2]^{1/2}$ (see Figure 4 of the main text). The D values after a particle deformation γ_{GNP} = 10 % (see main text) are reported in Table S6. Figure S21 depicts the Z-dependence of the unstretched ${h_{pol}}^2/b^2N_{arm}$ and stretched ${h'_{pol}}^2/b^2N_{arm}$ chain energy, with chain stretching being $\frac{{h'_{pol}}^2}{b^2N_{arm}} - {h_{pol}}^2/b^2N_{arm}$ for the same γ_{GNP} = 10 %.

Table S6. Characteristic sizes of the activated hopping model

M_{arm} [kg/mol]	D [nm]	R [nm]
196	26.2	29.1
170	25.0	27.7
130	22.9	25.4
94	20.6	22.9
48	16.7	18.6
33	14.9	16.6

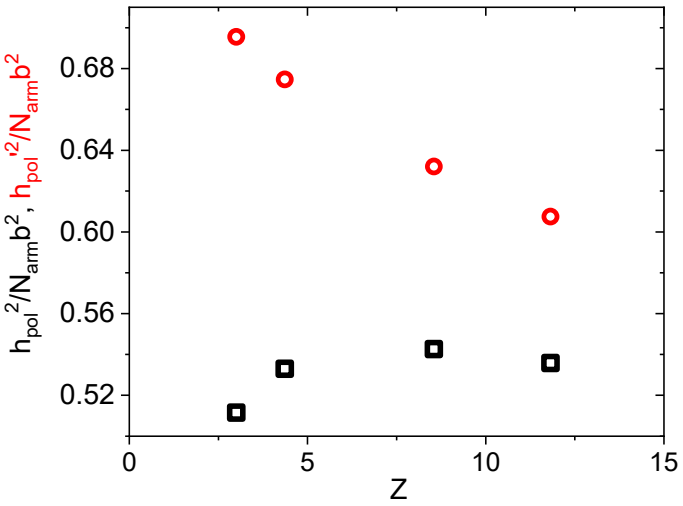

Figure S21. Z-dependence of ${h_{pol}}^2/b^2N_{arm}$ (black symbols) and ${h'_{pol}}^2/b^2N_{arm}$ (red symbols) used in the activated hopping model to describe the hopping potential.

A comparison is shown in Figure S22 between experiments and predictions, for the activated hopping potential against the number of entanglements Z (see discussion in the main text). This serves as a consistency check for this simple hopping model and the associated first-order guide to the cross-over between colloidal and polymeric regimes.

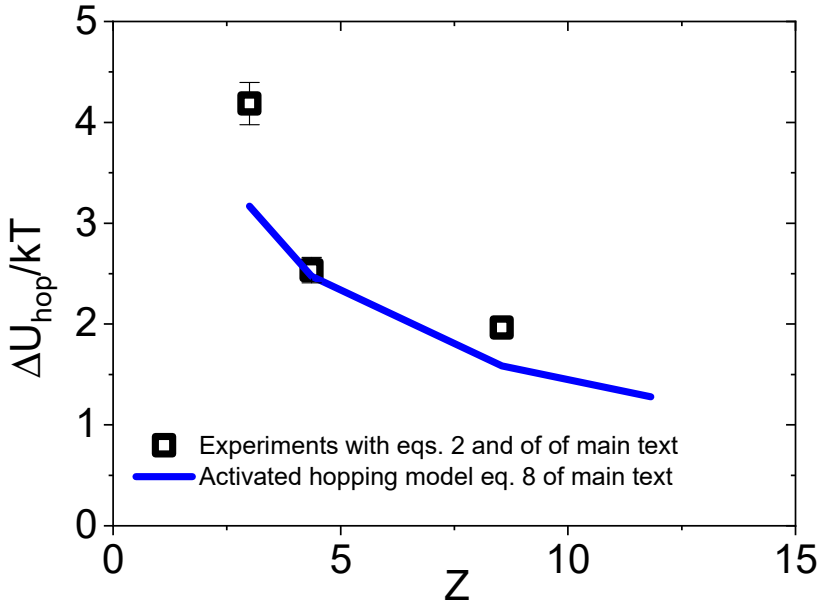

Figure S22. Activated hopping potential as a function of the number of entanglements per grafted arm. The symbols correspond to values extracted from rheological experiments (eq. 2 of the main text), the blue solid line represents the model prediction (eq. 8 of the main text). See also Table S7.

We report below the "chemistry parameter" $M=\left(\frac{3v_0}{4\pi b^3}\right)^{2/3}$ estimated for various chemistries reported in Figure 5 of the main text.

For PBD, v_0=0.21 nm^3, b=0.96 nm,[17] M=0.15

for PEO, v_0=0.21 nm^3 , b=1.1 nm,[34] M=0.12

for PI, v_0=0.23 nm^3 , b=0.82 nm,[34] M=0.21

for PMA v_0=0.673 nm^3, b=1.47 nm,[34] M=0.14

for PS v_0=1.234 nm^3, b=1.8 nm,[17] M=0.14

Considering the small variance of M, we took an average value of M=0.15

Experimental and predicted values are listed in Table S7 for ΔU_{hop} (based on the theoretical model of the potential barrier and eq.2 discussed in the main text) and τ_{term} from the slow mode analysis

reported in the main text. Table S8 lists the experimental normalized colloidal modulus $\frac{G_{LF}R^3}{kT}$ for both the GNPs and PBD stars (see also section 6 below) investigated, along with that predicted with *C*=5 (see main text).

Table S7. Quantities obtained from slow mode analysis

M_{arm} [kg/mol]	N_{arm} [-]	$\Delta U_{hop}/k_BT$ [-]	τ_{term} [s]
33	67	4.2	357140
48	96	2.5	294120
94	189	2.0	406500
130	263	-0.8	43333
33	67	3.2	361580
48	96	2.5	308900
94	189	1.6	105180
130	263	1.3	91160

Table S8. Experimental and predicted (with C=5) normalized colloidal modulus

Sample Code	$\frac{G_{LF}R^3}{k_BT}$ experiment	$\frac{G_{LF}R^3}{k_BT}$ prediction
GNPs		
94k	9.9	8.0
48k	18.2	12.7
33k	13.6	16.5
PBD stars (see also section 6 below)		
875	26.9	28.9
29	36.5	25.3
1114	62.1	77.2
2828	138.6	139

6. Linear viscoelastic master curves for multiarm star polymer melts

All the star polymer samples were made of polybutadiene (1,4-microstructure) and synthetic details were provided elsewhere.[39] The measurements involved conventional small-amplitude oscillatory shear (DFS) at different temperatures in the range -100 to 40 ºC, complemented in some cases by creep experiments (see also main text and Figures S4-S7 above). The linear viscoelastic spectra are depicted in Figure S24 for different stars (and a linear polymer for reference) from the literature[40,41] and for two new stars with f = 1114 and 2828 and respective M_{arm} = 1270 and 1300 g/mol. Their chemical core had an estimated radius of 5 nm.[25] The MM fits for polybutadiene (1,4-microstructure) stars are shown in Figure S25 for f = 929 (panel A) and 875 (panel B) and respective M_{arm} = 4000 and 5800 g/mol, taken from Ref. 41 at the same temperature difference from the glass transition T_g. Lastly, the extended spectrum for the star with f = 929, M_{arm} = 4000 g/mol from creep measurements[39] is shown in Figure S26 below. The experimental and predicted normalized low-frequency plateau moduli, according to eq. 12 of the main text, are listed in Table S8.

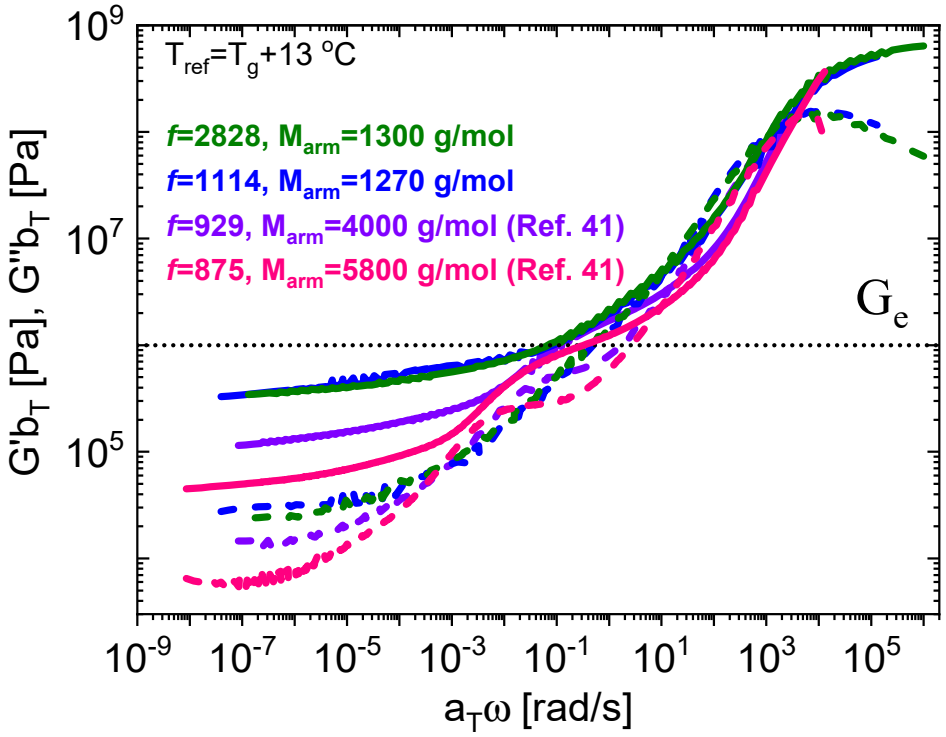

Figure S23. Linear viscoelastic master curves in terms of shifted $G'b_T$ (solid lines) and $G''b_T$ (dashed lines) as functions of the shifted frequency ωa_T for different multiarm polybutadiene (1,4-microstructure) stars, including those of Ref. 41 at the same temperature difference from the glass transition T_g. Details about the star synthesis can be found in Refs. 39-41. The dotted black line indicates the plateau modulus of polybutadiene chains in the molten state.[34]

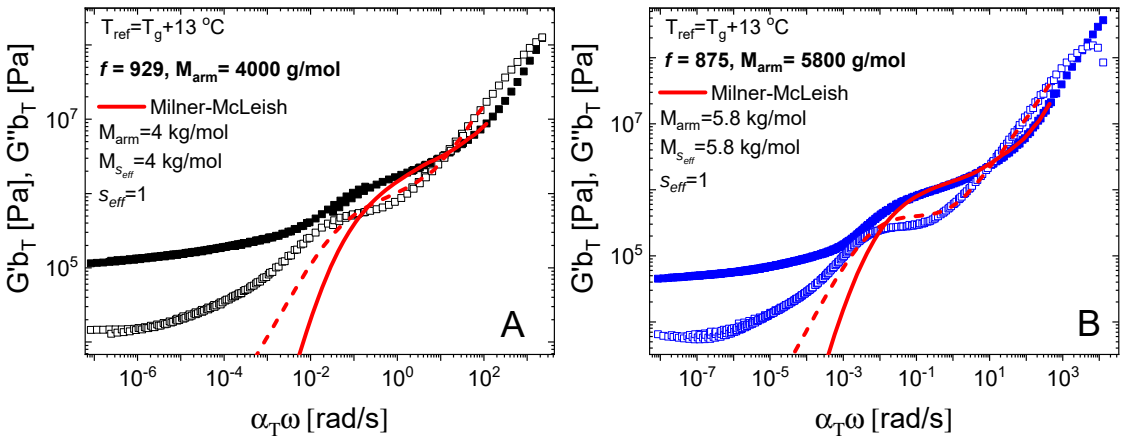

Figure S24. Linear viscoelastic master curves in terms of shifted $G'b_T$ (solid lines) and $G''b_T$ (dashed lines) as a function of the shifted frequency ωa_T for polybutadiene (1,4-microstructure) stars $f = 929$ (panel A) and 875 (panel B) and respective $M_{arm} = 4000$ and 5800 g/mol, taken from Ref. 41 at the same temperature difference from the glass transition T_g. The red lines represent the Milner-McLeish model in terms of storage modulus (solid line) and loss modulus (dashed line) with $s_{eff} = 1$ (note however that the applicability of this model in this situation with many short arms is questionable as already mentioned for the GNPs).

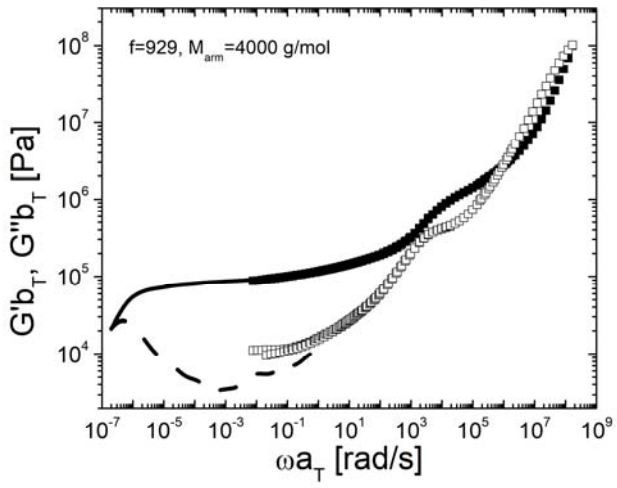

Figure S25. Linear viscoelastic master curves in terms of shifted $G'b_T$ and $G''b_T$ as a function of the shifted frequency ωa_T for a polybutadiene star previously studied by small amplitude oscillatory shear in Ref. 41: $f = 929$, $M_{arm} = 4000$ g/mol. The solid symbols are data obtained from DFS measurements and the lines represent the result of long-time creep measurements. The imperfect coincidence of G' is attributed to aging of the jammed state whose terminal relaxation is extremely slow and barely reached even by creep experiments (confirming the assignment to a jammed, i.e., solid-like state).

7. X-ray scattering analysis

Here we address the spatial organization of the GNP melts. The absolute scattered intensity, $I(q)$, was measured as a function of scattering wavevector q for the GNPs investigated in this work,[23] as shown in Figure S27A. As M_{arm} increases, the location of the structure peaks shifts to lower q values, suggesting that the inter-particle distance is increasing monotonically with the chain length. The data were reasonably well fitted in Fourier space using a polydisperse spherical form factor and a hard sphere interaction (Percus-Yevick) structure factor. The fitted values for the first peak of the inter-particle structure factor are well below the value of 2.85,[42] suggesting that these systems do not exhibit a strong long-range, crystalline-like order. The center-to-center distance of the particles can be estimated as 2π a $/q_{max}$ where q_{max} is the scattering wavevector at the maximum intensity, and the coefficient a, set to 1.23, reflects a structure controlled only by two-body correlation.[43] It follows that π a $/q_{max}$ relates to the particle radius. The center-to-center particle distance and the particles radius extracted from the X-ray experiments are reported in Figure 27B and contrasted with the particle radius calculated as per eq. S3. It is worth noticing the good agreement between the measured and estimated particle radii. The dependence of the particles center-to-center distance on the total particle size is depicted in Figure S28 for the GNPs, as well as for star polymers, some taken from the literature.[40] The data follow a 1/3 slope, which suggests that all these highly grafted spherical particles (GNPs and stars) in the melt are closely packed with a uniform spatial organization.[40]

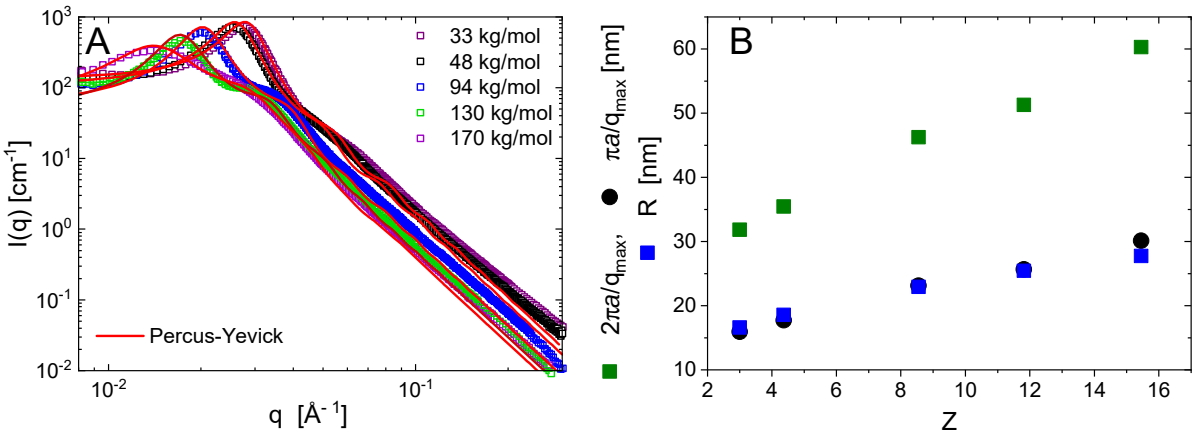

Figure S26. A) X-ray scattering intensity as a function of the scattering wavevector for the GNPs 33k-170k. The red solid lines represent fits to the data of a spherical polydisperse form factor and a hard sphere (Percus-Yevick) structure factor. B) Characteristic lengths as a function of the number of entanglements per arm. The green symbols represent the size extracted from the structural peak of panel A (see text) attributed to the center-to-center particle distance, the black symbols are half of the center-to-center particle distance (the particle radius), and the blue squares are the total radius of the particles estimated from eq. S1.

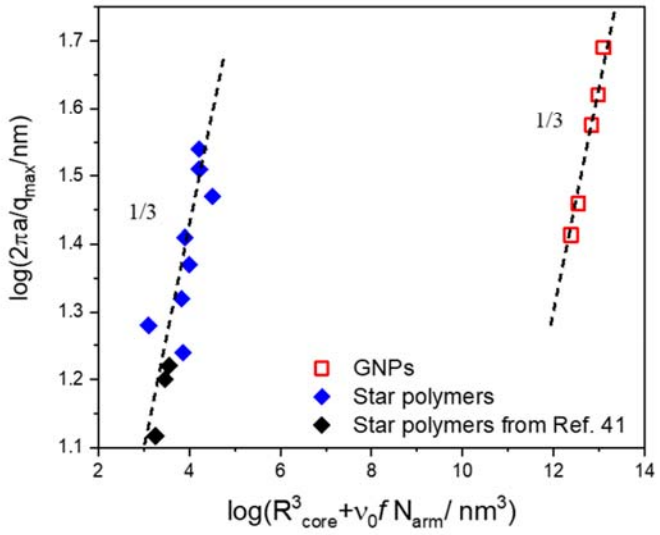

Figure S27. Logarithm of the center-to-center particle distance for star polymers (filled symbols) and GNPs (empty symbols) estimated as $2\pi a/q_{max}$ where q_{max} is the scattering wavevector at the maximum intensity, as a function of the logarithm of total particle size. The coefficient a was set to 1.23 for a structure controlled only by two-body correlation.[43] The 1/3 slope reflects a three-dimensional uniform packed arrangement of the nanoparticles.[40] The data for the stars taken from Ref. 40 are reported as black symbols.

References

(1) Midya, J.; Rubinstein, M.; Kumar, S. K.; Nikoubashman, A. Structure of Polymer-Grafted Nanoparticle Melts. *ACS nano* **2020**, *14* (11), 15505-15516.

(2) Ferry, J. D. *Viscoelastic Properties of Polymers*; John Wiley & Sons, 1980.

(3) Lixon, C.; Delpouve, N.; Saiter, A.; Dargent, E.; Grohens, Y. Evidence of Cooperative Rearranging Region Size Anisotropy for Drawn PET. *European Polymer Journal* **2008**, *44* (11), 3377–3384.

(4) Núñez, L.; Gómez-Barreiro, S.; Gracia-Fernández, C. A.; Nunez, M. R. Use of the Dielectric Analysis to Complement Previous Thermoanalytical Studies on the System Diglycidyl Ether of Bisphenol A/1, 2 Diamine Cyclohexane. *Polymer* **2004**, *45* (4), 1167–1175.

(5) Seyler, R. J. *Assignment of the Glass Transition*; Astm International, 1994.

(6) Gracia-Fernández, C. A.; Gómez-Barreiro, S.; López-Beceiro, J.; Saavedra, J. T.; Naya, S.; Artiaga, R. Comparative Study of the Dynamic Glass Transition Temperature by DMA and TMDSC. *Polymer Testing* **2010**, *29* (8), 1002–1006.

(7) Berriot, J.; Montes, H.; Lequeux, F.; Long, D.; Sotta, P. Evidence for the Shift of the Glass Transition near the Particles in Silica-Filled Elastomers. *Macromolecules* **2002**, *35* (26), 9756–9762.

(8) Kardasis, P.; Kalafatakis, N.; Gauthier, M.; Vlassopoulos, D.; Floudas, G. Layers of Distinct Mobility in Densely Grafted Dendrimer Arborescent Polymer Hybrids. *Physical Review Letters* **2021**, *126* (20), 207802.

(9) Schröter, K.; Wilde, G.; Willnecker, R.; Weiss, M.; Samwer, K.; Donth, E. Shear Modulus and Compliance in the Range of the Dynamic Glass Transition for Metallic Glasses. *The European Physical Journal B-Condensed Matter and Complex Systems* **1998**, *5* (1), 1–5.

(10) Geethamma, V. G.; Kalaprasad, G.; Groeninckx, G.; Thomas, S. Dynamic Mechanical Behavior of Short Coir Fiber Reinforced Natural Rubber Composites. *Composites Part A: Applied Science and Manufacturing* **2005**, *36* (11), 1499–1506.

(11) Donth, E. *The Glass Transition: Relaxation Dynamics in Liquids and Disordered Materials*; Springer Science & Business Media, **2013**.

(12) Van Gurp, M.; Palmen, J. Time-Temperature Superposition for Polymeric Blends. *Rheol Bull* **1998**, *67* (1), 5–8.

(13) Coppola, S.; Bacchelli, F.; Marrucci, G.; Ianniruberto, G. Rest-Time Effects in Repeated Shear-Startup Runs of Branched SBR Polymers. *Journal of Rheology* **2014**, *58* (6), 1877–1901.

(14) Trinkle, S.; Friedrich, C. Van Gurp-Palmen-Plot: A Way to Characterize Polydispersity of Linear Polymers. *Rheologica Acta* **2001**, *40* (4), 322–328.

(15) Trinkle, S.; Walter, P.; Friedrich, C. Van Gurp-Palmen Plot II–Classification of Long Chain Branched Polymers by Their Topology. *Rheologica Acta* **2002**, *41* (1–2), 103–113.

(16) Lohse, D. J.; Milner, S. T.; Fetters, L. J.; Xenidou, M.; Hadjichristidis, N.; Mendelson, R. A.; Garcia-Franco, C. A.; Lyon, M. K. Well-Defined, Model Long Chain Branched Polyethylene. 2. Melt Rheological Behavior. *Macromolecules* **2002**, *35* (8), 3066–3075.

(17) Rubinstein, M.; Colby, R. H. *Polymer Physics*; Oxford University Press New York, **2003**.

(18) Bacová, P.; Lentzakis, H.; Read, D. J.; Moreno, A. J.; Vlassopoulos, D.; Das, C. Branch-Point Motion in Architecturally Complex Polymers: Estimation of Hopping Parameters from Computer Simulations and Experiments. *Macromolecules* **2014**, *47* (10), 3362–3377.

(19) Honerkamp, J.; Weese, J. A Nonlinear Regularization Method for the Calculation of Relaxation Spectra. *Rheologica acta* **1993**, *32* (1), 65–73.

(20) Weese, J. A Regularization Method for Nonlinear Ill-Posed Problems. *Computer Physics Communications* **1993**, *77* (3), 429–440.

(21) Guth, E. Theory of Filler Reinforcement. *Journal of applied physics* **1945**, *16* (1), 20–25.

(22) Wolff, S.; Donnet, J.-B. Characterization of Fillers in Vulcanizates According to the Einstein-Guth-Gold Equation. *Rubber chemistry and technology* **1990**, *63* (1), 32–45.

(23) Buenning, E. Ph.D. Thesis. Controllable Free-Volume in Polymer-Grafted Nanoparticle Membranes: Origins, Characterization, and Applications. Columbia University, New York, **2018**.

(24) Cross, M. M. Rheology of Non-Newtonian Fluids: A New Flow Equation for Pseudoplastic Systems. *Journal of colloid science* **1965**, *20* (5), 417–437.

(25) Dukes, D.; Li, Y.; Lewis, S.; Benicewicz, B.; Schadler, L.; Kumar, S. K. Conformational Transitions of Spherical Polymer Brushes: Synthesis, Characterization, and Theory. *Macromolecules* **2010**, *43* (3), 1564–1570.

(26) Ohno, K.; Morinaga, T.; Takeno, S.; Tsujii, Y.; Fukuda, T. Suspensions of Silica Particles Grafted with Concentrated Polymer Brush: Effects of Graft Chain Length on Brush Layer Thickness and Colloidal Crystallization. *Macromolecules* **2007**, *40* (25), 9143–9150.

(27) Ohno, K.; Morinaga, T.; Takeno, S.; Tsujii, Y.; Fukuda, T. Suspensions of Silica Particles Grafted with Concentrated Polymer Brush: A New Family of Colloidal Crystals. *Macromolecules* **2006**, *39* (3), 1245–1249.

(28) Morinaga, T.; Ohno, K.; Tsujii, Y.; Fukuda, T. Structural Analysis of "Semisoft" Colloidal Crystals by Confocal Laser Scanning Microscopy. *Macromolecules* **2008**, *41* (10), 3620–3626.

(29) McConnell, G. A.; Lin, E. K.; Gast, A. P.; Huang, J. S.; Lin, M. Y.; Smith, S. D. Structure and Interactions in Tethered-Chain Systems. *Faraday Discussions* **1994**, *98*, 121–138.

(30) Wijmans, C. M.; Zhulina, E. B. Polymer Brushes at Curved Surfaces. *Macromolecules* **1993**, *26* (26), 7214–7224.

(31) Kapnistos, M.; Semenov, A. N.; Vlassopoulos, D.; Roovers, J. Viscoelastic Response of Hyperstar Polymers in the Linear Regime. *The Journal of chemical physics* **1999**, *111* (4), 1753–1759.

(32) Witten, T. A.; Leibler, L.; Pincus, P. A. Stress Relaxation in the Lamellar Copolymer Mesophase. *Macromolecules* **1990**, *23* (3), 824–829.

(33) Semenov, A. N. Rheology of Polymer Brushes: Rouse Model. *Langmuir* **1995**, *11* (9), 3560–3564.

(34) Fetters, L. J.; Lohse, D. J.; Colby, R. H. Chain Dimensions and Entanglement Spacings. In *Physical Properties of Polymers Handbook*; Mark, J. E., Ed.; Springer New York: New York, NY, 2007; pp 447–454.

(35) Walsh, D.; Zoller, P. *Standard Pressure Volume Temperature Data for Polymers*; CRC Press, 1995.

(36) Kapnistos, M.; Semenov, A. N.; Vlassopoulos, D.; Roovers, J. Viscoelastic Response of Hyperstar Polymers in the Linear Regime. *The Journal of chemical physics* **1999**, *111* (4), 1753–1759.

(37) Milner, S. T.; McLeish, T. C. B. Parameter-Free Theory for Stress Relaxation in Star Polymer Melts. *Macromolecules* **1997**, *30* (7), 2159–2166.

(38) Rubinstein, M.; Obukhov, S. P. Power-Law-like Stress Relaxation of Block Copolymers: Disentanglement Regimes. *Macromolecules* **1993**, *26* (7), 1740–1750.

(39) Gauthier, M.; Munam, A. Synthesis of 1, 4-Polybutadiene Dendrimer- Arborescent Polymer Hybrids. *Macromolecules* **2010**, *43* (8), 3672–3681.

(40) Pakula, T.; Vlassopoulos, D.; Fytas, G.; Roovers, J. Structure and Dynamics of Melts of Multiarm Polymer Stars. *Macromolecules* **1998**, *31* (25), 8931–8940.

(41) Gury, L.; Gauthier, M.; Cloitre, M.; Vlassopoulos, D. Colloidal Jamming in Multiarm Star Polymer Melts. *Macromolecules* **2019**, *52* (12), 4617-4623.

(42) Hansen, J.-P.; Verlet, L. Phase Transitions of the Lennard-Jones System. *Physical Review* **1969**, *184* (1), 151–161.

(43) Guinier, A. X-Ray Diffraction in Crystals, Imperfect Crystals and Amorphous Bodies, Ed. by WH Freeman and Co. *San Francisco* **1963**.